THE ASTROPHYSICAL JOURNAL, 503:396–414, 1998 August 10

GODDARD HIGH-RESOLUTION SPECTROGRAPH OBSERVATIONS OF COOL LOW-GRAVITY STARS. IV. A COMPARISON OF THE K5 III STARS α TAURI AND γ DRACONIS[1]

RICHARD D. ROBINSON
Computer Sciences Corporation, Code 681 NASA/Goddard Space Flight Center, Greenbelt, MD 20771; robinson@opal.gsfc.nasa.gov
KENNETH G. CARPENTER
Laboratory for Astronomy and Solar Physics, Code 681 NASA/Goddard Space Flight Center Greenbelt, MD 20771; carpenter@tma1.gsfc.nasa.gov
AND
ALEXANDER BROWN
CASA/University of Colorado, Campus Box 398, University of Colorado, Boulder, CO 80309-0389;
Received 1997 November 10; accepted 1998 March 19

ABSTRACT

The Goddard High-Resolution Spectrograph (GHRS) has observed the K5 III star α Tau in the 2330 Å region on three separate occasions. These spectra show marked changes with time, with the UV continuum varying by a factor of 2, and with the emission lines changing in flux by 30% or more, with the amount of change dependent upon the opacity of the line. The variations suggests a restructuring of the atmosphere rather than simply a change in the surface area covered by chromospheric material. Surprisingly, there was no detectable change in the chromospheric turbulence on timescales of hours or years. On average, the lower part of the atmosphere was found to be fairly static, with a slight infall of 1–2 km s^{-1}. At higher altitudes, probed by observation of the stronger Fe II lines as well as of the O I (UV 2) and Mg II (UV 1) resonance lines, there is evidence for the acceleration of a slow wind, similar to that seen in the M giants γ Cru and μ Gem. This wind is much less massive than for the later type giants, however, since its effects are seen in only the most optically thick of the Fe II lines. Comparison of the α Tau observations with similar data for the K5 III hybrid star γ Dra shows remarkable similarity in the photosphere and lower chromosphere. Both stars have pronounced UV continua, identical turbulences and chromospheric densities, and very similar line fluxes and profiles for all lines formed in the lower chromosphere, including C II], Co I, Si II], and Fe II. A deep exposure near 1500 Å also shows the first evidence for hot plasma in the atmosphere of α Tau through the detection of the C IV (UV 1) doublet with a surface flux about 30% of that observed in γ Dra. Most of the evidence for the stellar wind is in the Mg II (UV 1) and O I (UV 2) resonance lines. Modeling these lines using the Sobolev with Exact Integration (SEI) radiative transfer code shows that the wind in γ Dra accelerates faster and reaches a higher terminal velocity than does the wind in α Tau. However, the wind turbulent velocity in γ Dra is only about one-third of the value seen in α Tau. We conclude that the observations support the suggestion by Judge & Stencel that the processes that heat the chromosphere are distinct from those that drive the stellar winds.

Subject headings: stars: chromospheres — stars: individual (α Tauri, γ Draconis) — stars: late-type — stars: mass loss — ultraviolet: stars

1. INTRODUCTION

Luminous stars on the cool side of the Linsky-Haisch dividing line have been characteristically separated into two groups, noncoronal and hybrid. The noncoronal stars are typified by cool atmospheres, with temperatures less than 10^4 K and massive, low-speed winds with terminal velocities of ≤ 30 km s^{-1}. Hybrid stars, on the other hand, have hot transition regions and coronal plasmas as well as high-speed winds that can reach terminal velocities of 150 km s^{-1} or more (see, e.g., Hartmann, Dupree, & Raymond 1980). The term "hybrid" comes from the idea that the stars share the characteristics of both the coronal and noncoronal stars. This situation was considered to be unusual since the presence of closed magnetic fields, required for the presence of hot plasma, is generally thought to inhibit the formation of a cool wind. Recently, however, the existence of hot plasma in noncoronal stars has been found to be relatively common (see, e.g., Ayres et al. 1998), which raises the question of whether the hybrids are truly a separate class or are merely extreme examples in a population of stars having a continuous range of atmospheric characteristics.

Ignoring the presence of the hot plasma, the main difference between noncoronal and hybrid stars is the nature of their winds. By comparing the characteristics of pairs of hybrid and noncoronal stars that have the same spectral type, it may therefore be possible to obtain clues about the processes that drive these winds. With this in mind, we initiated a comparison of the K5 III stars α Tau and γ Dra using spectra obtained with the Goddard High-Resolution Spectrograph (GHRS) aboard the *Hubble Space Telescope*.

α Tau (Aldebaran = HR 1457) is a classic example of a noncoronal star. It is located well to the right of the coronal dividing line (which is near K2 for giant stars) and has a violet-red asymmetry in the Mg II resonance lines, which indicates a wind with a low terminal velocity (Judge 1986). This was the first cool star observed by the GHRS (Carpenter et al. 1991) and has been the subject of a number

[1] Based on observations with the NASA/ESA *Hubble Space Telescope*, which is operated by the Association of Universities for Research in Astronomy, Inc., under NASA contract NAS 5-26555.

of studies related to the dynamics and structure of stellar atmospheres (see, e.g., Judge 1986; Judge & Cuntz 1993). γ Dra (HR 6705), on the other hand, has a strongly asymmetric Mg II emission with two superimposed absorption features, one caused by absorption in the local interstellar medium (LISM) and the other formed near the terminal velocity of the wind. This is a characteristic signature of a hybrid star (Drake, Brown, & Linsky 1984). Brown et al. (1995) confirmed the hybrid nature of the star by detecting C IV in a GHRS spectrum. The surface flux was ∼20 times smaller than on the Sun and was at the time the smallest detected on any star.

In § 2 we describe the α Tau observations and the techniques used in the data reduction. In § 3 we discuss the properties of the two stars obtained from a review of the scientific literature. In §§ 4–8 we discuss the results of our analysis. Section 4 includes a discussion the UV continuum, and § 5 contains an examination of the evidence for hot plasma in α Tau from a deep exposure of the C IV lines near 1550 Å. In § 6 we study the chromospheric turbulence deduced from the C II] and other optically thin emission lines, and in § 7 we examine the atmospheric flows as deduced from the C II], Fe II, O I, and Mg II profiles. Finally, in § 8 we study the magnitude and the nature of the variations observed between the various α Tau data sets. In § 9 we examine the nature of the stellar winds for the two stars by empirically modeling the observed line profiles using the Sobolev with Exact Integration (SEI) radiative transfer code.

2. OBSERVATIONS AND DATA REDUCTION

The observations of α Tau were obtained on 1990 December 27, 1994 April 8, and 1996 October 15. The 1990 observations were part of the science assessment program for the GHRS and have been reported by Carpenter et al. (1991). The 1994 observations were designed to investigate the stellar atmospheric dynamics and will be the main subject of this paper. The 1996 observations were directed primarily at the study of fluorescent processes (McMurry et al. 1998) and will be analyzed in more detail in a subsequent paper. In the present paper, we will make a limited use of these later spectra to investigate time variations of the stellar line profiles. A summary of the relevant observations is presented in Table 1. The observations of γ Dra were obtained on 1991 April 18 and 1995 July 20 and will be discussed in detail in a later paper.

To ensure the greatest accuracy in both profile shape and measured radial velocities, both stars were observed through the 0.″22 Small Science Aperture (SSA), which is matched to the size of 1 resolution element on the detector. To overcome drifts of the spectra on the detector, caused primarily by thermal variations within the spectrograph and the interaction of the earth's magnetic field with the detector's control fields, we obtained wavelength calibration exposures of the on-board Pt lamps (referred to as WAVECALS) immediately prior to taking each stellar spectrum. We also broke each observation into a sequence of exposures, each having an integration time of 5 minutes or less. This allowed for the correction of any wavelength shifts that occurred during the observation sequence. With these precautions, we were able to establish a wavelength scale that is internally accurate (within an individual spectrum) to better than 0.05 diode widths and has an absolute accuracy of better than 0.3 diode widths. These correspond to internal and absolute accuracies of approximately 0.5 and 3.0 km s^{-1} for the medium-resolution gratings and 0.15 and 1.0 km s^{-1} for the echelle exposure at 2800 Å.

The spectra were reduced using the CALHRS procedure. This program combined the individual samples into a single spectrum, subtracted the background, corrected the effects of vignetting and the echelle blaze function (if required), and applied the current absolute flux calibration. The data are not expected to be photometrically accurate, since they

TABLE 1

GHRS OBSERVATIONS OF α Tau

Observation ID	Instrument Setup (Grating/Aperture)	Observation Start Time (UT)	Central Wavelength (Å)	Exposure Time (minutes)	Dispersion (Å $diode^{-1}$)
		1990 Nov 27			
Z0DD5106M	E-B/LSA	15:49:03	2327.1	14.8	0.025
Z0DD5108M	G270M/LSA	17:03:23	2345.2	4.9	0.095
Z0DD510FM.....	E-B/SSA	18:33:36	2327.1	54.3	0.025
Z0DD510KT	G270M/SSA	20:32:17	2345.2	20.1	0.095
		1994 Apr 8			
Z2890107T.....	G270M/SSA	01:21:17	2344.0	19.7	0.095
Z289010AT	G160M/SSA	02:57:48	1295.5	19.7	0.071
Z289010CT	G160M/SSA	03:23:35	1295.5	19.7	0.071
Z289010FT	G160M/SSA	04:42:30	1549.2	19.7	0.069
Z289010HT.....	G160M/SSA	05:08:11	1549.2	39.5	0.069
Z289010KT.....	G160M/SSA	07:47:23	1653.9	19.7	0.068
Z289010MT	G160M/SSA	08:13:11	1653.9	19.7	0.068
Z289010PT	G200M/SSA	09:31:47	1993.8	19.7	0.066
Z289010ST.....	G270M/SSA	11:00:29	2753.2	10.8	0.092
Z289010WT	E-B/SSA	11:20:11	2799.3	14.4	0.030
Z289010YT	G270M/SSA	12:36:59	2344.2	19.7	0.095
		1996 Oct 15			
Z3FX0207T.....	G270M/SSA	20:11:34	2344.7	13.4	0.095
Z3FX020BT	E-B/SSA	20:33:17	2798.9	12.6	0.030

were obtained through the SSA. However, on average the absolute fluxes should be good to better than 15%, while the relative fluxes of features within a given spectrum are accurate to better than 5%.

3. PROPERTIES AND EVOLUTIONARY STATUS OF THE PROGRAM STARS

In Table 2 we present a summary of the physical properties of α Tau and γ Dra as presented in the scientific literature. Both stars have a spectral classification of K5 III, with γ Dra being slightly hotter than α Tau. The angular diameters of the stars have been investigated using a variety of techniques and give reasonably consistent results. Combining these angular diameters with the distances recently obtained with *Hipparcos* then allows the determination of the radii, which are found to be typical for this spectral class. The radius and the effective temperature allow a determination of the bolometric luminosity through the relation $Ł_{\rm bol} = 4\pi R_*^2 \sigma T_{\rm eff}^4$. Gravities have been deduced primarily through spectroscopic analysis and are relatively uncertain, though γ Dra is typically found to have a larger gravity than α Tau. The measured radius and the gravity then allow an estimate of the stellar mass, though the large uncertainty in the gravity leads to large error bars. A refinement in the mass determination was proposed by el Eid (1994), who noted a correlation between the $^{16}O/^{17}O$ ratio and stellar mass for evolved stars. Using this ratio in conjunction with evolutionary calculations, el Eid (1994) found a mass of 3 $M_\odot$ for γ Dra and 1.5 $M_\odot$ for α Tau, in approximate agreement with the estimates based on stellar gravity. Finally, a comparison of the deduced luminosity and effective temperature with the evolutionary tracks (see, e.g., McWilliams 1990) indicates masses of 3.3 $M_\odot$ and 2.0 $M_\odot$ for γ Dra and α Tau, respectively.

The evolutionary state of the stars is still somewhat uncertain. El Eid (1994) estimates that γ Dra may be in the early helium shell burning stage, which would place it on the asymptotic giant branch (AGB). However, he admits that the $^{12}C/^{13}C$ ratio was somewhat large for this state of evolution. In an analysis of α Tau, Kovacs (1983) was unable to determine whether the star was still on the red-giant branch (RGB) or had evolved to the AGB.

4. CONTINUUM EMISSION

As mentioned above, α Tau and γ Dra have identical spectral types (K5 III) and similar optical and IR colors. To check whether this similarity extends to the UV, we measured the flux from selected regions of the GHRS spectra, which are relatively free of narrowband emission and absorption features, in order to estimate the strength of the UV continuum. In all cases, the count rates within these regions were at least 5 times larger than the measured background. These measured fluxes were corrected for the reddening toward each star, assuming the values of $E(B-V)$ given in Table 2, converted to surface flux using the angular diameters given in the same table, and then plotted in Figure 1*a*. The derived surface flux distributions for the two stars are nearly identical. The scatter of the points results from noise and small absorption features.

Figure 1*a* also shows the flux distribution predicted by a traditional Kurucz ATLAS9 photospheric model (Kurucz 1992) for a star with an effective temperature of 4000 K and log g of 1.5. The observed fluxes lie well above the traditional pure-photosphere model at all wavelengths below 3000 Å, suggesting that the excess emission comes from the nonradiatively heated region of the atmosphere. Following Morossi et al. (1993), we calculated several ATLAS9 models that used the same stellar parameters described above but were restricted so that the temperature never went below a specified "temperature minimum" ($T_{\rm min}$) value. As seen in

TABLE 2

PROPERTIES OF THE PROGRAM STARS

Property	α Tau	γ Dra	Reference
Spectral type	K5 III	K5 III	1
Distance (pc)[a]	20 ± 0.4	45.2 ± 0.9	
Angular diameter (mas)	20.9 ± 0.21	10.17 ± 0.1	2, 3, 4
Radius ($R_\odot$)[b]	44	49	
Effective temperature (K)	3898 ± 30	3985 ± 45	2, 5, 6
log g	1.25 ± 0.49	1.50 ± 0.39	6, 7, 8
Mass ($M_\odot$)[c]	1.5 ± 0.6	3.0 ± 0.5	7
$v \sin i$ (km s^{-1})	2.7	3.5	9
Photospheric turbulence (km s^{-1})	2.0 ± 0.2	2.0 ± 0.2	6
Johnson V	0.86	2.23	1, 4
M_V[d]	-0.65	-1.04	
$L_{\rm bol}$ ($L_\odot$)[e]	394 ± 15	535 ± 25	
$(B-V)_0$	1.54 ± 0.08	1.50 ± 0.08	1, 5, 8
$E(B-V)$	0.006	0.015	4
log [Fe/H]	-0.34 ± 0.21	-0.14 ± 0.16	8, 10, 11
$^{16}O/^{17}O$	600^{+300}_{-150}	300^{+100}_{-75}	7, 12
$^{12}C/^{13}C$	9 ± 1	13 ± 2	7

[a] *Hipparcos* observations.
[b] Calculated from distance and angular diameter.
[c] From gravity and radius.
[d] From distance and Johnson V magnitude.
[e] From $T_{\rm eff}$ and radius.

REFERENCES.—(1): Jaschek 1982; (2): Cohen et al. 1996; (3): Blackwell et al. 1990; (4): Di Benedetto 1993; (5): Flower 1996; (6): Bonnell & Bell 1993; (7): el Eid 1994; (8): Cayrel de Strobel et al. 1992; (9): Rutten & Pylyser 1988; (10): McWilliams 1990; (11): Taylor 1991; (12): Smith & Lambert 1985.

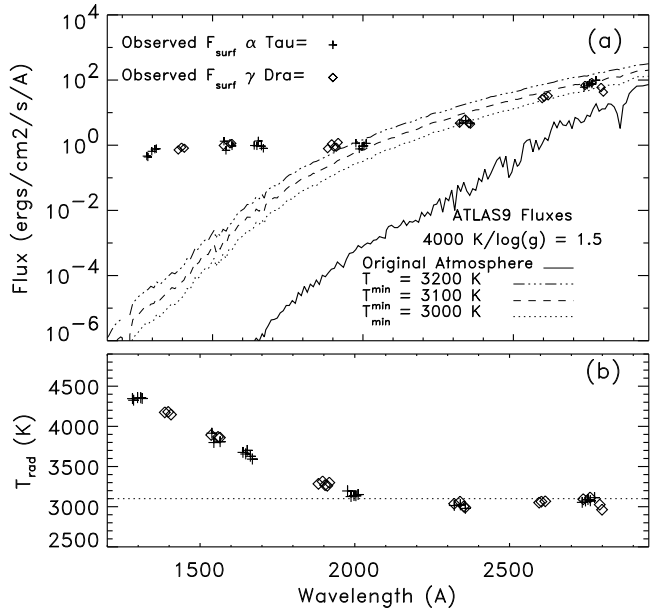

FIG. 1.—(*a*) Comparison of continuum fluxes seen in α Tau and γ Dra. The observed fluxes have been dereddened and converted to surface fluxes. The solid line shows the expected photospheric flux from a K5 III star, as calculated by Kurucz, while the dashed lines show flux distributions computed assuming three different values of T_{min}, as described in the text. (*b*) Effective radiation temperature for the observed UV continuum samples.

Figure 1*a*, the inclusion of a T_{min} layer at the top of the model significantly improves the agreement of the computed and observed fluxes down to about 2300 Å, suggesting that the 2300–3000 Å fluxes are produced in a temperature-minimum region having $T_{min} \sim 3050$ K. This is somewhat hotter than previously inferred from analysis of the wings of the Ca II H and K lines (Kelch et al. 1978).

The far-UV (FUV) flux clearly requires that the continuum be formed in the region of rising temperatures in the lower chromosphere. This is illustrated in Figure 1*b*, which shows the effective radiation temperature (T_{rad}) as a function of wavelength. Here T_{rad} is inferred by setting the Planck function, πB, equal to the surface flux at a given wavelength and then solving for the corresponding temperature. Note that the minimum radiation temperature corresponds to the value of T_{min} required by the ATLAS9 calculations.

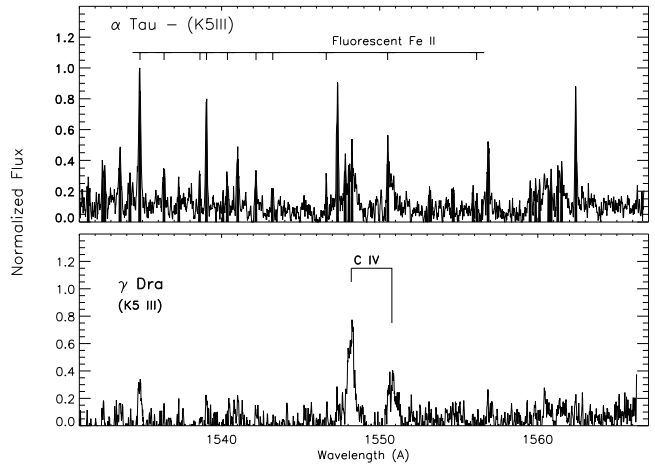

FIG. 2.—CIV wavelength region in (*upper panel*) α Tau, observed in 1994, compared with that in (*lower panel*) γ Dra, observed in 1996.

Traditionally, radiative losses from the chromosphere are assumed to come from the strong chromospheric emission lines, such as the resonance line of Mg II and Ca II (see, e.g., Linsky 1991). The existence of a relatively strong chromospheric continuum emission suggests an additional source of radiative losses, which should be considered when evaluating nonradiative heating processes. To evaluate the importance of this emission, we interpolated the observed continuum samples over the wavelength range between 1300 and 3000 Å and then determined the excess flux by integrating between the theoretical photospheric fluxes and the observations. The total emission from α Tau was found to be 9.5×10^{-10} ergs cm^{-2} s^{-1}, which translates into a surface flux of 4×10^5 ergs cm^{-2} s^{-1}. For comparison, the integrated flux from the Mg II h and k lines from α Tau was only 1.5×10^{-10} ergs cm^{-2} s^{-1}, or about 15% of the continuum emission. Clearly the losses from this excess UV emission are important.

5. A SEARCH FOR HOT PLASMA

The traditional view has been that cool, noncoronal stars such as α Tau lack significant amounts of plasma at transition-region or coronal temperatures (Linsky & Haisch 1979). To check this assertion, we took a deep exposure of α Tau centered on 1550 Å to look for the presence of the C IV lines, formed near temperatures of $\sim 10^5$ K. The resultant spectrum is shown in Figure 2, along with a similar exposure of γ Dra. The C IV line was clearly detected in the α Tau spectrum, with an integrated flux of $(9.5 \pm 2) \times 10^{-14}$ ergs cm^{-2} s^{-1} from the doublet, corresponding to a surface flux of 37 ± 8 ergs cm^{-2} s^{-1}. The large uncertainty is caused by the numerous emission and absorption features that are blended with the lines. The absorption features are not caused simply by noise, since they repeat when the observation sequences are divided into two segments and compared. The lines producing these absorption features have not yet been identified. However, besides C IV, there are no other strong high-temperature lines within this wavelength region. The small widths of the absorption lines also suggests that they are formed at relatively low temperatures. The most likely interpretation is that the hot transition region material in α Tau is embedded in much cooler plasma. Velocities measured by fitting a Gaussian profile to the C IV lines show that they are essentially at rest with respect to the star.

For γ Dra, the observed integrated C IV doublet flux was $6.4 \pm 0.4 \times 10^{-14}$ ergs cm^{-2} s^{-1}. Converting this to surface flux using the measured angular diameter (Table 2) gives 122 ± 8 ergs cm^{-2} s^{-1}, which is 3.5 ± 1.0 times larger than the α Tau surface flux.

The major difference between the two spectra in Figure 2 is the presence of numerous narrow emission lines in the α Tau spectrum. These have previously been reported by Carpenter & Robinson (1995) and have been identified as fluorescent H_2 and Ca II recombination lines (McMurry et al. 1996) as well as fluorescent Fe II lines excited by Lyα radiation. A preliminary report on these and other fluorescent processes seen in α Tau is given by McMurry et al. (1998).

6. TURBULENCE

Optically thin emission lines typically have very narrow intrinsic widths and are not subject to opacity broadening. For these reasons, their profiles are highly influenced by

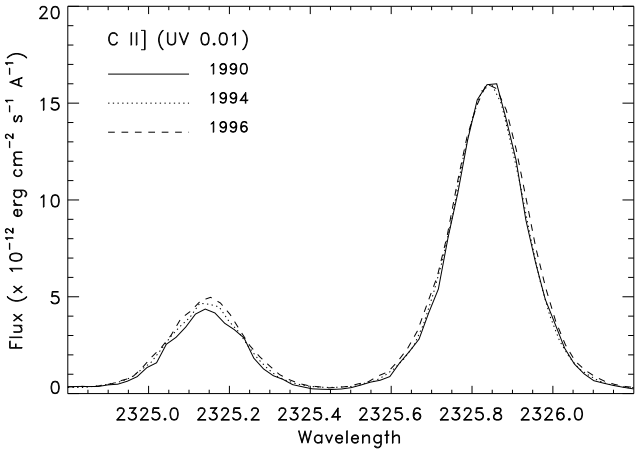

FIG. 3.—Comparison of two C II] intercombination lines observed from α Tau in 1990 (*solid line*), 1994 (*dotted line*), and 1996 (*dashed line*). The fluxes have been normalized so that the peak flux of the 2325.4 Å line in the 1990 and 1996 data matches that in the 1994 data.

Doppler shifts, and they are good diagnostics of both microscopic and macroscopic turbulence. The intercombination lines of C II] near 2325 Å are particularly useful in this regard and have been previously studied by Carpenter et al. (1991) to investigate the turbulence in α Tau. Simple Gaussian fits to the function $\exp[-(v/v_0)^2]$ show a characteristic velocity (v_0) of 14 km s^{-1} (FWHM = 24 km s^{-1}), while more detailed fitting showed that the wings of the profile were enhanced relative to a simple Gaussian profile. Carpenter et al. (1991) originally interpreted this as indicating the presence of a higher velocity component to the turbulence. Later analysis (see, e.g., Carpenter & Robinson 1997) has shown that the shape can be the result of an anisotropic velocity distribution in which the turbulence at any given location on the surface is preferentially directed either along or perpendicular to the radial direction (see, e.g., Gray 1992). If we assume no limb darkening, then the profile can be explained by anisotropic turbulence with $v_0 = 25$ km s^{-1}. A more realistic assumption for the optically thin C II] lines is that limb brightening exists because of the larger path length near the limb. In our calculations, we assumed that the intensity varies as $\sim\cos^{-1}\theta$, where θ is the angle of observation. For turbulence directed perpendicular to the radial direction, the limb

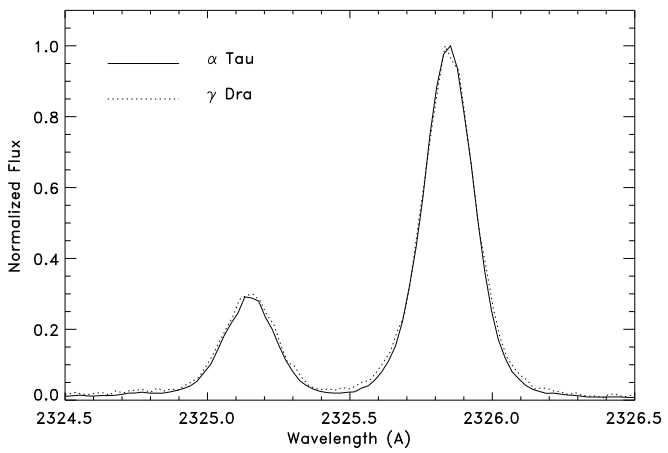

FIG. 4.—Comparison of profiles for several C II] intercombination lines as observed in α Tau and γ Dra. The lines have been normalized so that the peak flux of the 2325.4 Å line matches.

TABLE 3

PROPERTIES OF SIMPLE EMISSION LINES

Line ID	Lab Wavelength (Å)	Radial Velocity (km s^{-1})	FWHM (km s^{-1})
S I (UV 9)	1295.653	57 ± 2	37. ± 2
S I (UV 9)	1296.174	59 ± 2	40. ± 2
Fe II.....	1289.094	56 ± 2	24 ± 2
Fe II.....	1292.406	57 ± 2	24 ± 2
Fe II.....	1293.593	58 ± 2	23 ± 2
C I.....	1993.620	56 ± 2	16 ± 3
C II] (0.01).....	2323.500	56 ± 2	25 ± 2
C II] (0.01).....	2324.689	59 ± 1	24 ± 1
C II] (0.01).....	2325.398	58 ± 1	24 ± 1
C II] (0.01).....	2328.122	59 ± 2	23 ± 2
Co II (UV 8).....	2330.370	54 ± 2	22 ± 1
Si II (0.01).....	2350.17	57 ± 2	21 ± 2

brightening will enhance the wings of the observed profile and reduce the required value of v_0 to 21 km s^{-1}. For radially directed turbulence, the core is enhanced and a larger velocity ($v_0 = 28$ km s^{-1}) is required. Finally, when regions of both radial and tangentially directed turbulence are present with equal probability, then the effects of limb brightening will cancel and the required turbulent velocity is the same as when no limb brightening is considered (i.e., $v_0 = 25$ km s^{-1}). The chromospheric turbulence is large compared with the photospheric turbulence (~ 2 km s^{-1}; Bonnell & Bell 1993) and is probably related to the chromospheric heating.

In Figure 3 we compare the profiles of two C II] lines observed in 1994 with the same lines observed in the 1990 data. The integrated C II] line fluxes in 1994 were found to be more than 30% larger than in the 1990 data. However, when the 1990 data is scaled so that the integrated flux matches the 1994 data, the profiles for the two data sets agree almost exactly. This indicates that while there were significant changes in the atmosphere between 1990 and 1994, the average chromospheric turbulence remained constant.

A variety of other lines are also suitable for this analysis, including the Si II] λ2350 intercombination line, the radiatively excited lines Co II λ2330 and Ni II λ2367, and the leakage line C I λ1993. The results of fitting these lines are presented in Table 3 and generally agree with the velocities and widths derived from the C II] lines. The only exceptions are the S I lines, which may be optically thick and therefore subject to opacity broadening, and the C I line, which has a slight absorption blend on the blue side, reducing the width somewhat.

A popular theory for chromospheric heating involves acoustic shock waves generated by convective motions (see, e.g., Ulmschneider 1991). These shocks interact with one

TABLE 4

C II] FLUX RATIOS AND ELECTRON DENSITIES

Flux Ratio	α Tau[a] 1990	α Tau[a] 1994	α Tau[a] 1996	γ Dra[a] 1996
R1 = $F_{2325.4}/F_{2328.1}$.....	3.1 (9.05)	3.1 (9.05)	2.9 (9.15)	2.9 (9.15)
R2 = $F_{2325.4}/F_{2326.9}$.....	5.1 (8.8)	5.1 (8.8)	5.2 (8.85)	5.5 (8.9)
R3 = $F_{2324.7}/F_{2326.9}$.....	1.4 (8.8)	1.5 (8.9)	1.6 (9.0)	1.6 (9.0)
log average density.....	8.90	8.92	9.02	9.03

[a] Numbers in parenthesis indicate estimates of log N_e derived using the expressions from Lennon et al. 1985.

another and can occasionally reach large amplitudes, which could possibly be detected as changes in the profile of these optically thin lines. To search for such variations, we obtained an exposure of C II] at the beginning of the 1994 program and a second at the end, approximately 8 hr later. The two spectra show no significant differences. This may simply indicate that the timescale for variations is longer than the 8 hr sample or that we happened to be observing during a particularly quiet time. Each of the three C II] exposures taken in 1994 represented the sum of four individual 5 minute integrations. As explained above, these were taken so that short term drifts of the spectrum could be identified and removed in the reduction process. These spectra were calibrated individually and compared in order to search for any short-term variations that might be averaged out during the longer integrations. As might be expected, no statistically significant deviations were found.

In Figure 4 we compare the scaled C II] profiles of γ Dra with the 1994 α Tau data. Here the stellar radial velocities have been removed and the fluxes have been normalized to 1 at the peak of the 2325 Å line. The C II] line ratios are slightly different in the two stars, suggesting a chromospheric density for γ Dra that is about 10% larger than in α Tau (see Table 4). The deduced turbulence is also slightly larger in γ Dra, with a characteristic velocity of ~ 28 km s^{-1} (neglecting limb brightening). Overall, however, the two stars show remarkably similar characteristics.

7. PLASMA FLOWS

7.1. *Optically Thin lines*

The radial velocities deduced from fitting the relatively simple profiles of the optically thin lines (see § 6) are given in Table 3. In nearly all cases, the lines show redshifts with respect to the stellar rest frame (which has a radial velocity [RV] of $+54$ km s^{-1}), in agreement with earlier results by Carpenter et al. (1991).

7.2. Fe II *Lines*

Bulk flows in the upper layers of the chromosphere are often identifiable in the cores of optically thick, centrally reversed emission lines. In the second paper of this series, Carpenter, Robinson, & Judge (1995; hereafter Paper II) used the strong absorption components of a large number of Fe II lines in the UV spectrum of the M giant γ Cru to confirm that the base of the stellar wind lies in the stellar chromosphere and to trace the acceleration of that wind from a few km s^{-1} to approximately 14 km s^{-1}. To search for these flows in α Tau, we have adopted the same method of parameterizing the line profiles as used in Paper II. The emission wings were fitted with a single Gaussian component. We then assumed that the central absorption feature is generated within an overlying slab of material. The absorption coefficient within this slab was assumed to have a Gaussian shape with a specified optical depth and radial velocity. The assumed line profile is then expressed as (see Carpenter & Robinson 1997)

$$I(\lambda) = I_0 \exp\left[-\frac{(\lambda-\lambda_w)^2}{\Delta\lambda_w^2}\right] \exp\left[-\tau(\lambda)\right] \qquad (1)$$

and

$$\tau(\lambda) = \tau_0 \exp\left[-\frac{(\lambda-\lambda_c)^2}{\Delta\lambda_c^2}\right], \qquad (2)$$

where λ_w and $\Delta\lambda_w$ are the central wavelength and width of the wing profile and λ_c, $\Delta\lambda_c$, and τ_0 are the central wavelength, width, and line center opacity, respectively, of the optical depth profile within the absorbing slab. In many cases, a single absorbing slab was insufficient to account for the highly asymmetric absorption cores of the lines, and a second slab at a different λ_c was introduced, as was the case for the previous analysis of γ Cru. The results of fitting all unblended, self-reversed emission lines in the α Tau spectra are presented in Table 5.

The velocities deduced from the Fe II lines are plotted in Figure 5 as a function of the relative optical depths of the lines, derived in the same manner as described in Paper II. Basically, it is assumed that the lines of higher optical depth will probe higher in the stellar atmosphere, so that a relation between the velocity of a central absorption component and line strength reflects a wind acceleration with height. A comparison of Figure 5 with the results for γ Cru (Fig. 10 of Carpenter et al. 1995) shows a number of similarities and differences. In both cases, the emission wings show a slight inflow with respect to the photosphere. For the weakest lines, this inflow velocity is approximately independent of line strength, averaging about 1–2 km s^{-1}. For the strongest lines, however, the deduced inflow increases to nearly 4 km s^{-1}, or about the same as that seen in the C II] lines. This implies that the wings are formed low in the atmosphere. α Tau also shows the same blueward drift in the position of the central absorption feature with increasing line strength as seen in the γ Cru data. However, in the case of α Tau, these shifts appear only in the most optically thick lines, while thinner lines show either an unreversed profile or an unshifted central reversal. A comparison of Fe II profiles seen in α Tau and γ Cru shows that the line wings have about the same width, implying a similar chromospheric structure. The weaker wind signature in α Tau therefore suggests that the wind has a much smaller optical depth and, consequently, is much less massive than that of γ Cru.

In Figure 6 we compare a variety of Fe II line profiles from the 1994 spectra of α Tau and the 1996 spectrum of γ Dra. Overall, these profiles are very similar, with γ Dra

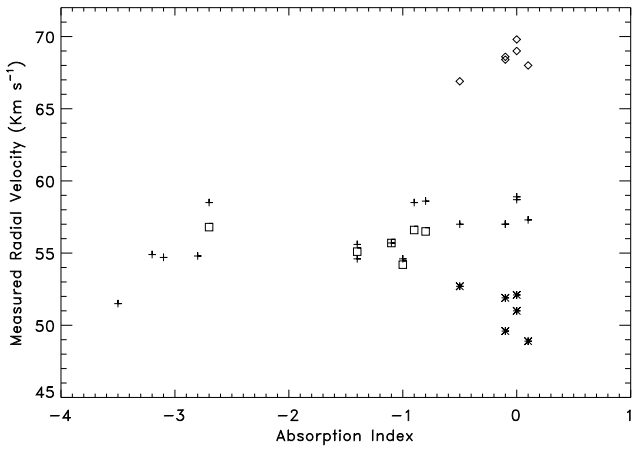

FIG. 5.—Measured velocities of different components of selected Fe II emission lines as a function of the opacity of the lines (see § 7.2). Squares indicate Gaussian fits to unreversed lines. Crosses indicate the wing velocity for centrally reversed lines; asterisks represent the strong blueshifted absorption component; and diamonds indicate the weaker redshifted absorption component.

TABLE 5

FITS TO SELF-REVERSED EMISSION LINES

UV Multiplet Number	Wavelength (Å)	log (*gf*)	Radial Velocity (km s^{-1})			FWHM (km s^{-1})			Optical Depth	
			Emission	abs1	abs2	Emission	abs1	abs2	abs1	abs2
					Fe II					
3	2332.800	−0.19	57.3	48.9	68.0	0.38	0.23	0.12	1.4	0.1
3	2338.008	−0.34	57.0	51.9	68.6	0.38	0.22	0.13	1.3	0.4
3	2364.829		58.7	54.7	...	0.40	0.25	...	1.2	...
32	2732.446	−3.35	54.7	...	...	0.20	...	...	...	...
32	2759.332		54.9	...	...	0.18	...	...	...	...
32	2775.338		51.5	...	...	0.14	...	...	...	...
35	2331.307	−0.68	57.0	52.7	66.9	0.36	0.20	0.12	1.0	0.2
35	2354.889	−2.76	58.5	56.8	...	0.31	0.20	...	0.7	...
35	2362.020	−0.93	58.6	56.5	...	0.33	0.20	...	0.7	...
35	2366.593		58.5	56.6	...	0.30	0.22	...	0.7	...
62	2730.734	−0.64	55.7	55.7	...	0.28	0.18	...	0.6	...
62	2755.737	0.43	58.9	51.0	69.8	0.49	0.25	0.15	1.3	0.5
63	2736.968		54.6	54.2	...	0.30	0.23	...	1.0	...
63	2739.548	0.32	57.0	49.6	68.4	0.47	0.25	0.15	1.2	0.5
63	2761.813	−0.87	55.6	55.1	...	0.30	0.20	...	0.3	...
63	2768.935	−0.92	54.6	...	...	0.31	...	...	...	...
260	2741.395		54.8	...	...	0.21	...	...	...	...
					O I					
2	1302.168	−0.612	58.9	28.9	67.2	0.30	0.11	0.15	2.8	2.3
2	1304.858	−0.835	57.3	36.9	66.8	0.26	0.16	0.13	2.7	1.4
2	1306.029	−1.312	56.9	42.3	68.3	0.25	0.18	0.13	2.0	0.9

showing evidence for an outflow only in the strongest lines. In fact, the profile differences between the Fe II lines in the two stars are less than the changes seen in α Tau between the 1990 and 1994 data sets (see § 8). The ratio of the surface flux of the lower chromospheric lines in α Tau to that from γ Dra ranges between 0.6 and 0.8, suggesting that the chromosphere of the hybrid is slightly stronger than in the noncoronal star. However, given the variability seen in the α Tau spectrum (§ 8) and the known chromospheric variability of hybrids (Brown et al. 1996), it is possible that this observed difference is not significant.

7.3. *The* O I *and* Mg II *Lines*

The O I (UV 2) and Mg II (UV 1) resonance lines are some of the strongest emission features in the UV spectrum of K giants. These lines have very large optical depths and probe atmospheric heights well above those accessible to the Fe II lines. In Figure 7 we overplot the three O I (UV 2) lines and the strongest Fe II line, which has approximately the same shape in the two stars. For α Tau, the lines become progressively more asymmetric as the line strength increases. The position of the central absorption feature also progressively shifts to the blue, suggesting an accelerating wind. To quantify this behavior, we used the line-fitting procedure discussed in § 7.2. The results are presented in Table 5 and indicate outflow velocities up to −25 km s^{-1}. Note that the fits require both blue- and redshifted absorption features. The Mg II (UV 1) lines in α Tau (Fig. 8*b*) are not suitable for analysis because of the effects of LISM absorption at an RV of −30 km s^{-1} as well as a possible mutilation by overlying Mn I and Fe I in the blue wing of the k line (see, e.g., Robinson & Carpenter 1995), producing a pronounced kink in the profile.

The situation is somewhat different for γ Dra. In this case, there is evidence for absorption in the far blue wing of the lines, so that the O I and Fe II profiles tend to overlap in that region (note that the strong 1302 Å profile actually lies inside of the others). This absorption develops into a pronounced dip centered at −60 km s^{-1} in the blue wing of the Mg II (UV 1) lines. A similar, though weaker, feature is seen in the 1302 Å line of O I. This absorption is characteristic of hybrid stars and marks the terminal velocity of the wind. Note that as the lines strengthen they loose their blue peak and become progressively more mutilated on the blue side of the line, while the red side remains relatively constant. The strong absorption feature centered at 15 km s^{-1} in the 1302 Å line results from absorption within the LISM, while the narrow absorption features centered at ∼40 km s^{-1} in all three O I lines are caused by geocoronal O I.

In Figure 8*a*, we compare the 1302 Å lines in α Tau and γ Dra. Note that the red wings agree reasonably well with one another and that the blue wings also agree at outflow velocities greater than −80 km s^{-1}. This suggests that the intrinsic wing profiles are identical and that the major difference between the two stars is the degree of absorption in the core and near–blue wing. The O I (UV 2) and Mg II (UV 1) profiles in γ Dra can not be represented as a superposition of Gaussian profiles, so the analysis used in § 7.2 is no longer appropriate. An alternative method for examining the character of the wind incorporates the fact that the line wings are formed low in the atmosphere and that the broadening mechanisms are symmetrical (see, e.g., Carlsson & Judge 1993). The intrinsic line-wing profiles should therefore have a reflection symmetry about the radial velocity of the plasma in which the wings are formed. From the analysis presented in § 7.2, we know that the lower atmosphere has a moderately constant inflow velocity of approximately 1–2 km s^{-1}. If we assume that the asymmetry in the core is caused by overlying material within the wind, then we can roughly establish the amount of mutilation by reflecting the red wings of the profile about an RV of ∼2 km s^{-1}. The degree of mutilation can be quantified by assuming that

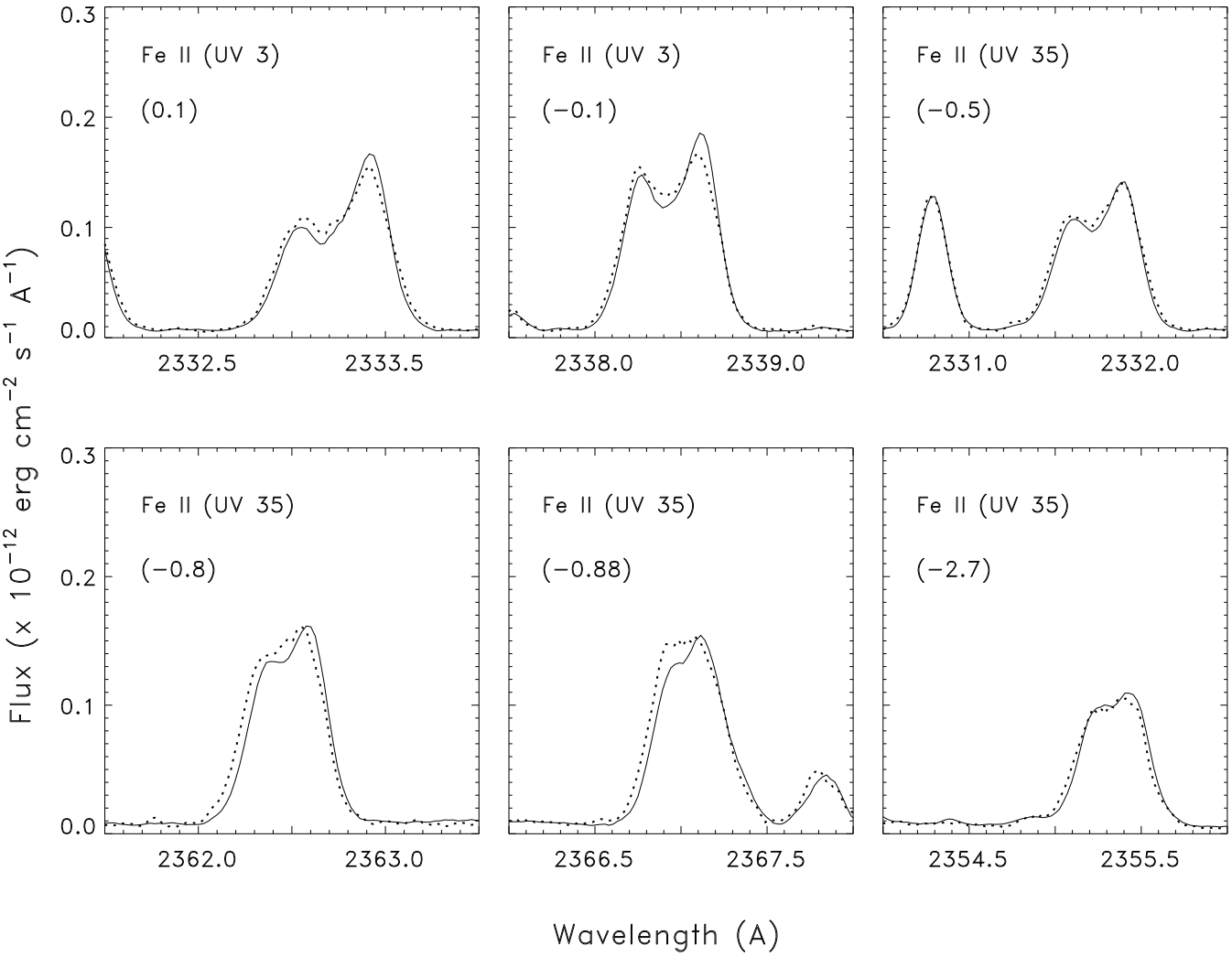

FIG. 6.—Fluxes of Fe II line profiles observed on α Tau in 1994 (*solid lines*) compared with those seen from γ Dra in 1996 (*dotted lines*). Numbers in parentheses in the upper left-hand corners represent the log of the effective optical depth of the lines, as defined in Carpenter et al. (1995). The fluxes for γ Dra have been adjusted so that the lines have the same integrated flux as those in α Tau.

the observed blue-wing flux at a given velocity [$I_b(v)$] is related to the red-wing flux at that velocity [$I_r(v)$] through the relation

$$I_b(v) = I_r(v) \exp\,[-\tau(v)]\,, \qquad (3)$$

where $\tau(v)$ represents a suppression factor that is related to the optical depth of overlying material traveling at velocity v (see, e.g., Mullan, Carpenter, & Robinson 1998). This is not *exactly* true, since some of the photons scattered out of the blue wing will reappear in the core and the red wing of the line. However, the expected red-wing enhancements are relatively small compared to the blue-wing absorption (see § 9), so the analysis is valid as a first approximation. The values of $\tau(v)$ empirically derived from the O I (UV 2) and Mg II (UV 1) lines in both α Tau and γ Dra are presented in Figure 9. For α Tau, these functions are broad and roughly symmetrical about a velocity of $\sim$30 km s^{-1}. There is some indication of opacity at velocities as high as 70 km s^{-1}. However, this signature may be spurious, since it is possible that the far blue wing of the profile is affected by geocoronal O I absorption. As expected, the derived optical depth increases with the strength of the line.

For γ Dra, the opacity distributions are skewed to higher velocities than in α Tau. The distributions derived from the Mg II h and k lines are sharply peaked with an opacity ratio of approximately 2:1, as expected from the relative line strengths. The distributions derived from the O I lines in γ Dra have a similar skew to the Mg II distributions but tend to peak at a slightly lower velocity and are much flatter near the peak than are the Mg II distributions. The interpretation of these empirical opacity distributions in the context of specific wind models will be discussed in § 9.

Finally, it is worth noting the presence of a narrow absorption feature in the Mg II h and k lines of α Tau at the rest velocity of the star. This feature is too narrow to be resolved in the lower resolution Fe II and O I observations of the star. The absorption appears to be moderately stable, since it appears in data sets taken more than 2 yr apart (see Fig. 10), and must originate well above the stellar chromosphere, since it shows up as an absorption feature in the most optically thick portion of the line. This feature probably represents absorption within a region of interaction between the stellar wind and interstellar material. This is similar to the hydrogen wall absorption reported by Wood

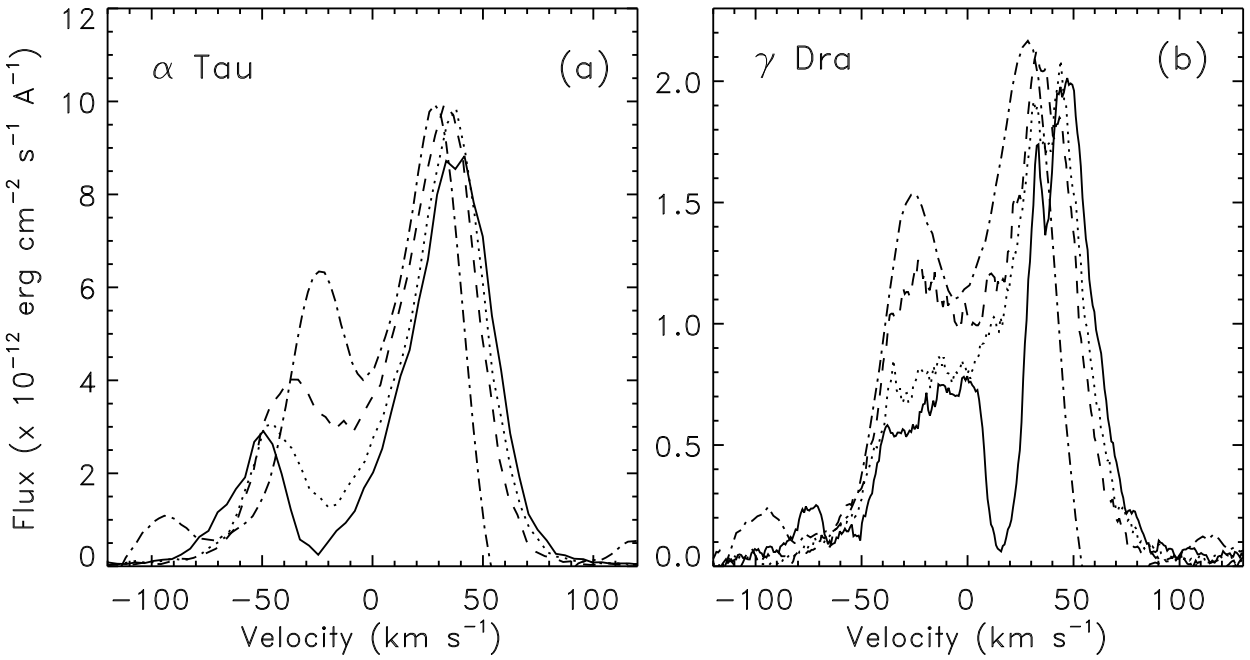

FIG. 7.—(*a*) Comparison of O I (UV 2) λ1302 (*solid line*), λ1304.9 (*dotted line*), and λ1306 (*dashed line*) profiles seen in α Tau in 1994. Velocities refer to the rest frame of the star, assuming a RV of +54 km s^{-1}. Also shown is the high-opacity Fe II (UV 62) 2755 Å line (*dot-dashed line*), which has had its flux adjusted to match the peak of the O I profiles. (*b*) O I (UV 2) and Fe II λ2755 profiles seen in γ Dra assuming a stellar radial velocity of −28 km s^{-1}. The line styles are the same as in (*a*).

& Linsky (1998) for the stars 61 Cyg A and 40 Eri A. There is no indication of a similar absorption in the Mg II observations of γ Dra and, to our knowledge, nothing similar has ever been reported in the Mg II profiles for any other star.

8. FLUX VARIATIONS

Thus far α Tau has been observed with the GHRS on three separate occasions in the 2330 Å region and twice at 2800 Å (see § 2). This allows us to roughly examine long-term variations in the line fluxes for Mg II, C II], Fe II, and Si II, as well as changes in the strength of the UV continuum in two well-separated wavelength regions. The results are summarized in Table 6. A significant uncertainty in these data comes from the fact that the spectra were obtained through the SSA, which is not a photometric aperture. We note, however, that the *relative* fluxes within a given spec-

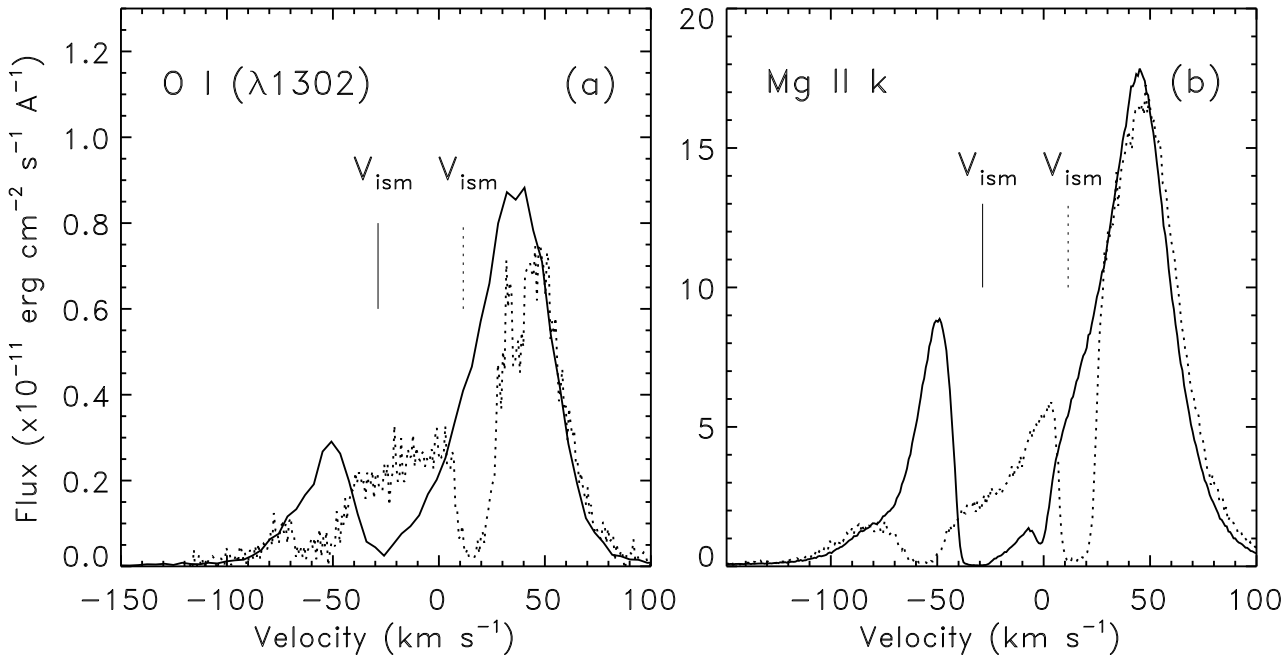

FIG. 8.—Comparison of (*a*) O I λ1302 and (*b*) Mg II k profiles observed on α Tau (*solid lines*) and γ Dra (*dotted lines*). The γ Dra fluxes have been scaled by a factor of 4, which is the square of the ratio of the observed stellar diameters The velocity of the LISM in the direction of each of the stars is indicated.

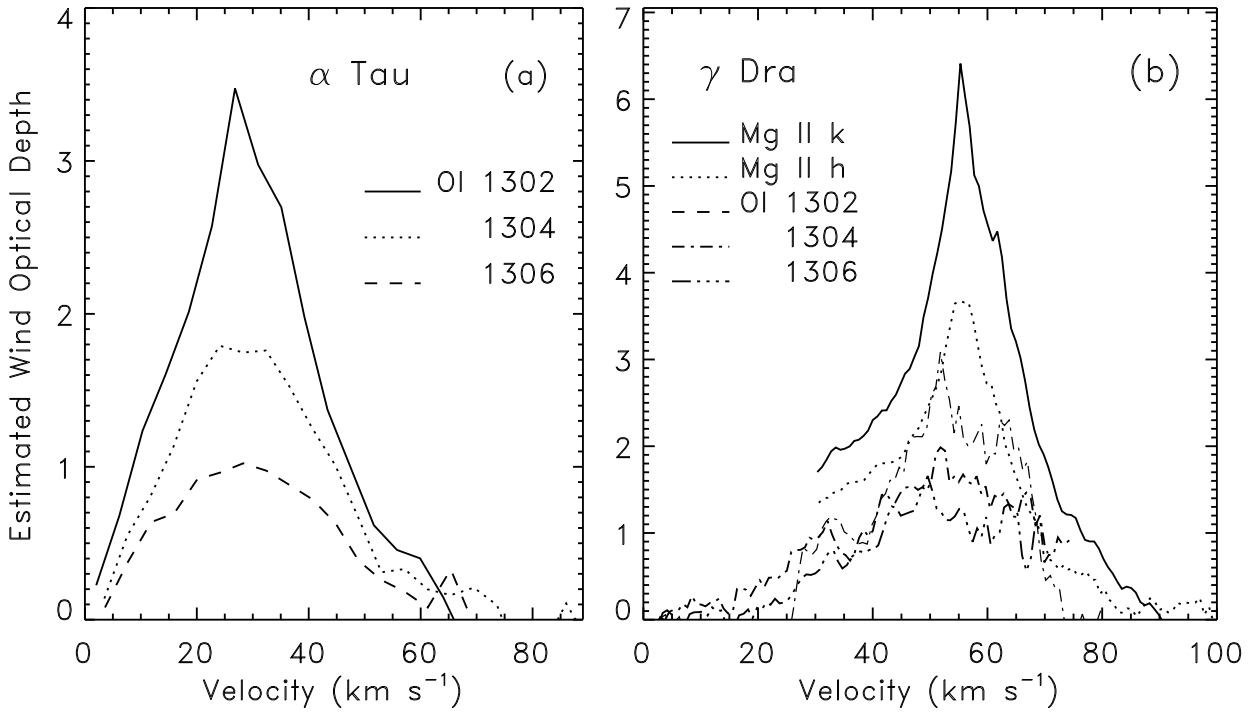

FIG. 9.—Empirical optical depth vs. velocity as derived from the reflection analysis discussed in § 7.3. (*a*) Results for α Tau as deduced from the O I (UV 2) multiplet lines. (*b*) Results for γ Dra using both the O I (UV 2) multiplet and the Mg II h and k lines.

trum should be accurate to within a few percent (see, e.g., Heap et al. 1995). Thus, an inaccurate centering of the star in the aperture or a difference in the stellar point-spread function (PSF) (e.g., in the pre-COSTAR observations taken in 1990 vs. post-COSTAR data taken after 1993 December) would produce a constant flux ratio (independent of wavelength) between two observations.

The continuum in the 2300 Å region was determined at 11 spectral regions that were chosen because they were free of obvious emission or absorption features. These regions covered a total of 9.2 Å, which is approximately 20% of the total range of wavelengths covered by the observation. The total number of counts within these regions was determined for each spectrum, the background was subtracted, and an average flux and uncertainty were derived using the appropriate calibration tables (see, e.g., Heap et al. 1995). In all cases, the measured background level was more than an order of magnitude less than the continuum level and agreed with the empirical background model derived by Lindler & Heap (1995).

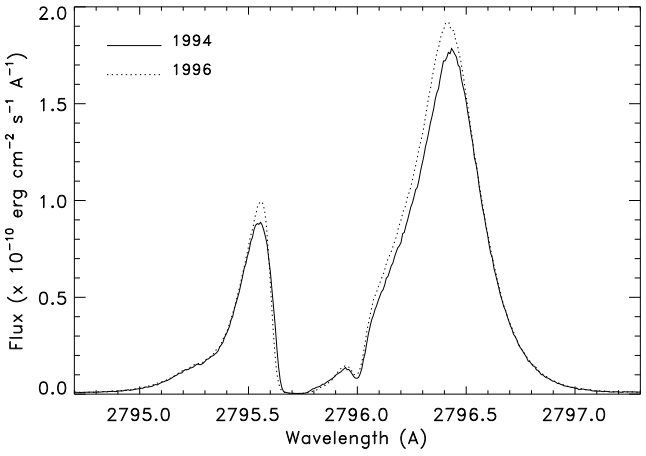

FIG. 10.—Mg II k profiles observed from α Tau in 1994 (*solid line*) and 1996 (*dotted line*).

As seen in Table 6, the continuum fluxes at both 2300 and 2800 Å in 1994 were approximately 17% larger than those seen in 1996. These differences are probably due to inaccuracies in centering the target. In 1990, however, the 2300 Å continuum was down by a factor of 2 from the other observations. The reality of these changes is suggested by the fact that variations in the emission line fluxes between 1990 and later times are significantly different from the changes observed in the continuum levels.

The line fluxes presented in Table 6 were determined by fitting a second-order polynomial to the continuum samples and then directly integrating each line profile above this continuum level. The uncertainties were determined assuming Poisson statistics for both the integrated line counts as well as the background and continuum levels. There are two important points to note from these measurements. First, if we assume that the continuum variations are real, then the data indicate that the line fluxes increased by 10%–30% in 1994 and 1996 relative to 1990. However, if the continuum variations are spurious, then normalizing the line fluxes to their respective continuum levels indicates a flux decrease of 30%–40% in 1994 and 1996 relative to 1990. In either case, the magnitude of the variations is large. Second, the changes in line fluxes depend on the line observed, which implies changes in the atmospheric structure rather than merely a change in the filling factor of the chromospheric plasma.

One of the most noticeable changes occurs in the C II] intercombination lines, which show a substantial change in the relative line intensities. These lines are often used as

TABLE 6

FLUX VARIATIONS IN α TAU

WAVELENGTH (Å)	LINE ID	INTEGRATED FLUX[a]			FLUX RATIOS[b]	
		1990	1994	1996	(1994/1990)	(1996/1990)
2320–2360.....	Continuum	0.69 ± 0.03[c]	1.44 ± 0.07[c]	1.22 ± 0.07[c]	2.09 ± 0.1	1.77 ± 0.1
2790–2805.....	Continuum	...	11.8 ± 0.5[c]	9.9 ± 0.5[c]	...	...
2323.5	C II]	1.5 ± 0.15	1.9 ± 0.12	1.8 ± 0.1	1.27 ± 0.08	1.20 ± 0.07
2324.7	C II]	9.7 ± 0.7	13.3 ± 1.0	13.1 ± 1.0	1.37 ± 0.1	1.35 ± 0.1
2325.4	C II]	35.8 ± 1.5	46.2 ± 1.5	43.3 ± 1.4	1.29 ± 0.04	1.21 ± 0.04
2326.9	C II]	7.1 ± 1.0	9.1 ± 1.0	8.3 ± 1.0	1.28 ± 0.14	1.17 ± 0.14
2328.1	C II]	11.6 ± 1.3	14.9 ± 1.3	14.8 ± 1.3	1.28 ± 0.1	1.28 ± 0.1
2330.4	Co II	3.9 ± 0.2	4.8 ± 0.2	4.6 ± 0.2	1.23 ± 0.05	1.18 ± 0.05
2331.3	Fe II	9.4 ± 0.4	11.3 ± 0.4	10.4 ± 0.4	1.20 ± 0.04	1.11 ± 0.04
2332.8	Fe II	11.4 ± 0.4	14.3 ± 0.4	12.5 ± 0.4	1.25 ± 0.03	1.10 ± 0.03
2334.4,.6	Si II	17.7 ± 0.5	22.4 ± 0.5	22.3 ± 0.5	1.27 ± 0.03	1.26 ± 0.03
2338.0	Fe II	13.4 ± 0.4	16.5 ± 0.4	15.0 ± 0.4	1.23 ± 0.03	1.12 ± 0.03
2348.3	Fe II	13.9 ± 0.4	17.4 ± 0.4	16.3 ± 0.4	1.25 ± 0.03	1.17 ± 0.03
2350.2	Si II	6.1 ± 0.2	7.4 ± 0.2	7.8 ± 0.2	1.21 ± 0.03	1.27 ± 0.03
2354.9	Fe II	6.2 ± 0.2	8.1 ± 0.2	8.0 ± 0.2	1.31 ± 0.03	1.29 ± 0.03
2362.0	Fe II	10.5 ± 0.3	12.7 ± 0.3	12.0 ± 0.3	1.21 ± 0.03	1.14 ± 0.03
2364.8	Fe II	6.4 ± 0.2	7.7 ± 0.2	7.4 ± 0.2	1.20 ± 0.03	1.16 ± 0.03
2366.6	Fe II	10.1 ± 0.3	12.6 ± 0.3	11.8 ± 0.3	1.25 ± 0.03	1.17 ± 0.03
2367.4	Ni II	1.1 ± 0.2	1.6 ± 0.2	1.3 ± 0.2	1.45 ± 0.18	1.18 ± 0.18

[a] Flux in units of 10^{-13} ergs cm^{-2} s^{-1}.
[b] Fluxes were uncorrected for continuum level.
[c] Flux in units of 10^{-13} ergs cm^{-2} s^{-1} Å^{-1}.

chromospheric density diagnostics, and the relative line ratios are consistent with an increase in electron density from 1990 ($N_e \sim 1.0 \times 10^9$ cm^{-3}) through 1996 ($N_e \sim 1.4 \times 10^9$ cm^{-3}), assuming the curves presented in Lennon et al. (1985) (see Table 4). Using the same analysis on γ Dra shows a density of 1.6×10^9 cm^{-3}.

An examination of the line profiles can indicate whether there were changes in turbulence or flows associated with the atmospheric restructuring discussed above. In § 6 we mentioned that the C II] line profiles show no discernible changes in the line profiles with time, implying that the chromospheric turbulence is nearly constant. In Figure 11 we compare a range of Fe II profiles, normalized so that the peak fluxes are of comparable intensity. There is no indication of shifts in the velocities or widths of these lines. The major changes occurs in the line cores, especially for intermediate opacity lines, which have much more symmetrical profiles and weaker central reversals in 1994 and 1996 than in 1990. Since this asymmetry marks the atmospheric flows, this observation implies that the wind is slightly variable. This variability is also shown by the changes in the cores of the Mg II lines (see Fig. 10).

9. DISCUSSION

9.1. *Wind Modeling Considerations*

In order to provide a more quantitative comparison of the winds seen in α Tau and γ Dra, we have performed some simple wind modeling using the SEI computer code described by Lamers, Cerruti-Sola, & Perinotto (1987). This code solves the radiative transfer equation in a homogeneous, spherically expanding atmosphere using a source function that is derived using the Sobolev approximation. Basically, this approximation assumes that the atmospheric turbulence is small compared to the gradient in the local flow velocity, so that different atmospheric layers are not coupled through velocity effects. Normally the Sobolev assumption is applied to the winds of hot stars, where the terminal velocity can exceed several thousand km s^{-1}. The SEI code has an advantage over approaches using a pure Sobolev approximation, however, in that the turbulence is explicitly taken into account in the radiative transfer. The program can therefore handle cases in which the turbulent velocity (v_D) is a large fraction of the wind terminal velocity (v_∞) provided the thermalization length within the wind is large, e.g., as in the case of pure photon scattering assumed here. To show this, Lamers et al. (1987) have run SEI simulations in which the parameter ω_D ($=v_D/v_\infty$) has a value ranging from 0.01 to 0.3 and compared the results with both an escape-probability method employing a pure Sobolev calculation (Castor 1970) and a more accurate comoving-frame method (e.g., Hamann 1980). The SEI calculations differ significantly from a pure Sobolev approximation for values of ω_D exceeding 0.02. However, the SEI method was shown to agree with the comoving-frame method for a wide variety of wind characteristics and optical depths. The main discrepancy was that SEI slightly underestimated the number of photons scattered into the red wing for lines with very large optical depths and large values of ω_D.

Since only the O I and Mg II resonance lines are strongly affected by the wind, we assume that the total column depth of the wind is small. This assumption is supported by the parameterizations obtained in the wing reflection analysis in § 7.3, which show that the effective optical depth for Mg II is less than 6 even for the hybrid star. A small optical depth in the wind implies a small density and a correspondingly small thermalization probability. We therefore assume in our calculations that the source function in the wind is completely determined by conservative scattering and that O I and Mg II are the dominate ionic species throughout the wind region. These are the same assumptions employed by Harper et al. (1995) in modeling the atmosphere of the hybrid star α TrA.

Before modeling the stellar profiles, it is worth examining the effects of various model parameters. First, we adopt the velocity (v) versus height (R) relation used by Castor & Lamers (1979),

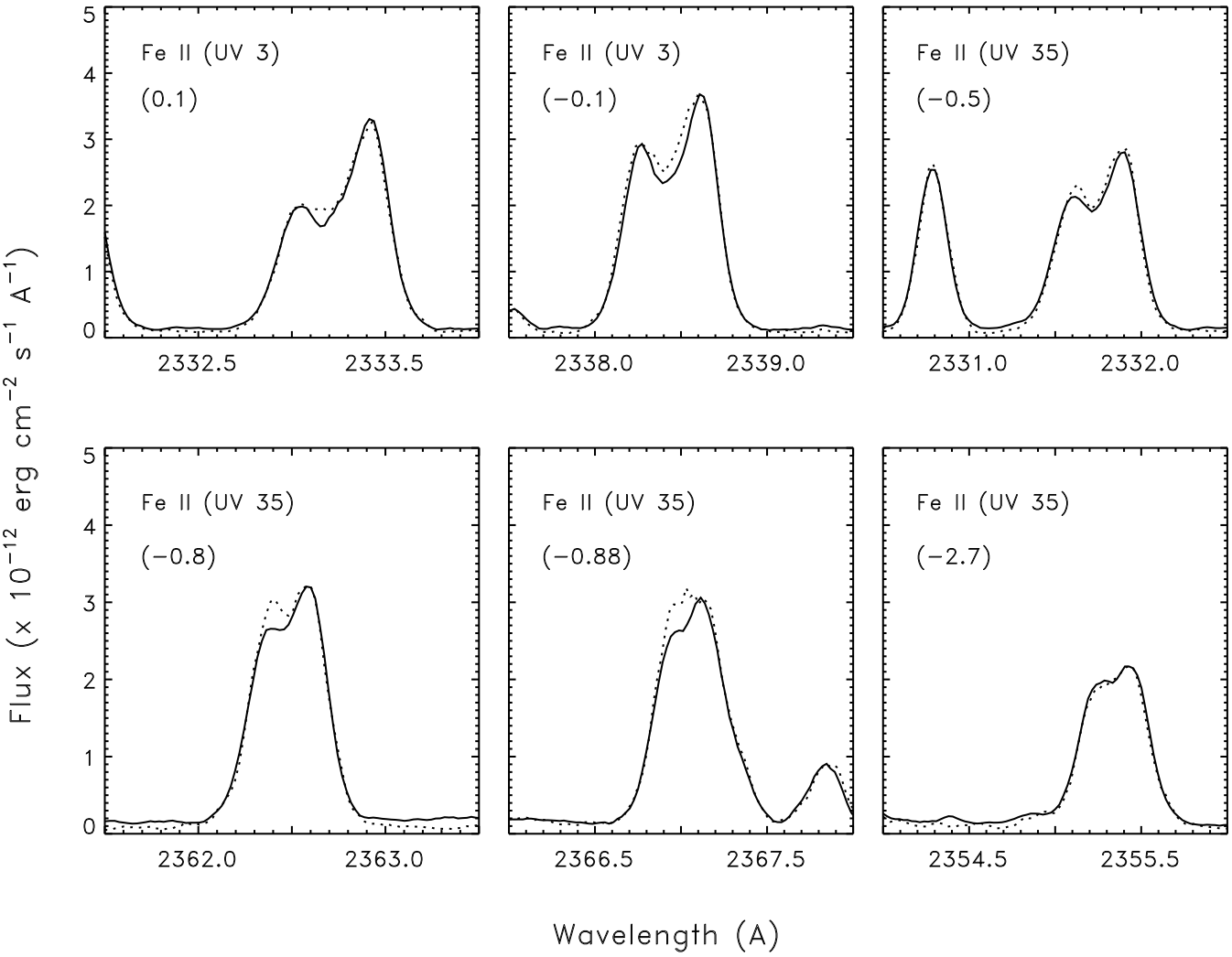

FIG. 11.—Comparison of Fe II line profiles from α Tau seen in 1990 (*solid lines*) with those from 1994 (*dotted lines*). Numbers in parentheses in the upper left-hand corners represent the log of the effective optical depth of the lines, as defined in § 7.2.

$$\frac{v(R)}{v_\infty} = 0.01 + 0.99\left(1 - \frac{R_*}{R}\right)^\beta , \tag{4}$$

where v_∞ is the terminal velocity of the wind, R_* is the stellar radius, and β is a constant that specifies the degree of acceleration of the wind. In this expression, it is assumed that $R/R_* \geq 1$ and $v/v_\infty \leq 1$. The relation is shown in Figure 12*a* for various values of β.

To simplify the problem, we assume that the wind is homogeneous, spherically symmetric, and isothermal, so that the ionization fraction of Fe II, O I, and Mg II is constant with height. Assuming conservation of mass, we can then write

$$\dot{M} = 4\pi R^2 \rho(R) v(R) = \text{constant} , \tag{5}$$

where $\dot{M}$ is the mass-loss rate and $\rho(R)$ is the mass density at height R. The opacity-height relation, $\tau(R)$, for a given spectral line is defined along the line of sight and is expressed as (see, e.g., Castor & Lamers 1979)

$$\tau(R) = \frac{\pi e^2}{mc} \frac{gf\lambda_0 N_i(R)}{U} \left(\frac{dR}{dv}\right), \tag{6}$$

where g, f, and λ_0 (in cm) are the statistical weight, oscillator strength, and central wavelength for the spectral line, $N_i(R)$ (in cm^{-3}) is the number density of the observed element with the required ionization stage, and U is the relevant partition function. Thus, $\tau(R)$ can be calculated using the velocity-height relation $[v(R)]$ given in equation (4) and the density distribution $[\rho(R)]$ obtained from equation (5). Given our assumptions, the shape of the opacity distribution is then entirely dependent upon the value of β, while the total wind opacity is determined by the mass-loss rate.

The influence of the wind is understood in terms of the classical P Cyg effect. Here photons traveling in the direction of the observer are scattered out of the line of sight by interactions in the wind and result in a blueshifted absorption component. At the same time, photons traveling at an angle to the line of sight can be scattered toward the observer by the wind, resulting in an increased emission in the line center and near–red wing. These effects are illustrated in Figure 13, which examines the influence of the wind optical depth and the acceleration parameter β (eq. [4]) on the line profile. Here we have followed the example of Harper et al. (1995) in prescribing a symmetric, intrinsic emission profile that is assumed to be generated within the lower chromosphere at the base of the wind. For $\beta = 1$, the optical depth of the wind decreases with increasing velocity (Fig. 12*b*). In this case, a low-opacity wind will preferentially

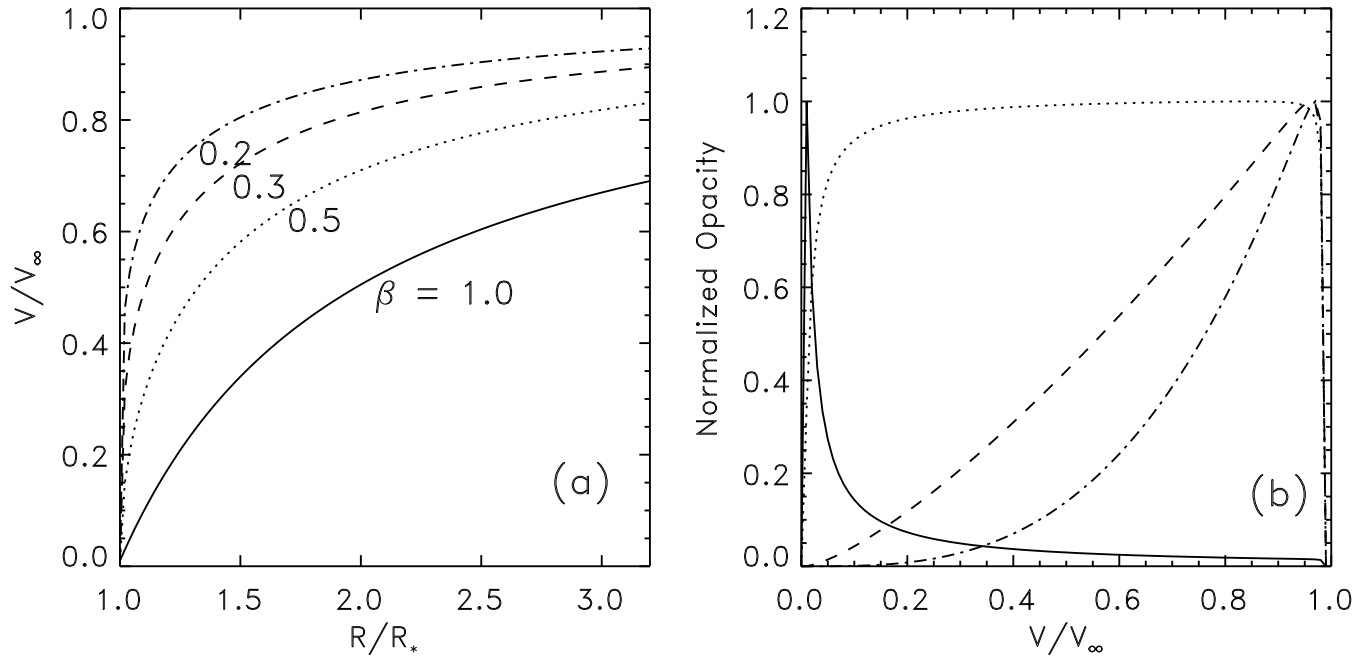

FIG. 12.—(*a*) Run of velocity with height for different values of β, as defined by eq. (4). (*b*) Wind opacity as a function of velocity for different values of β. These relations assume a constant mass flux with height, as discussed in § 9.

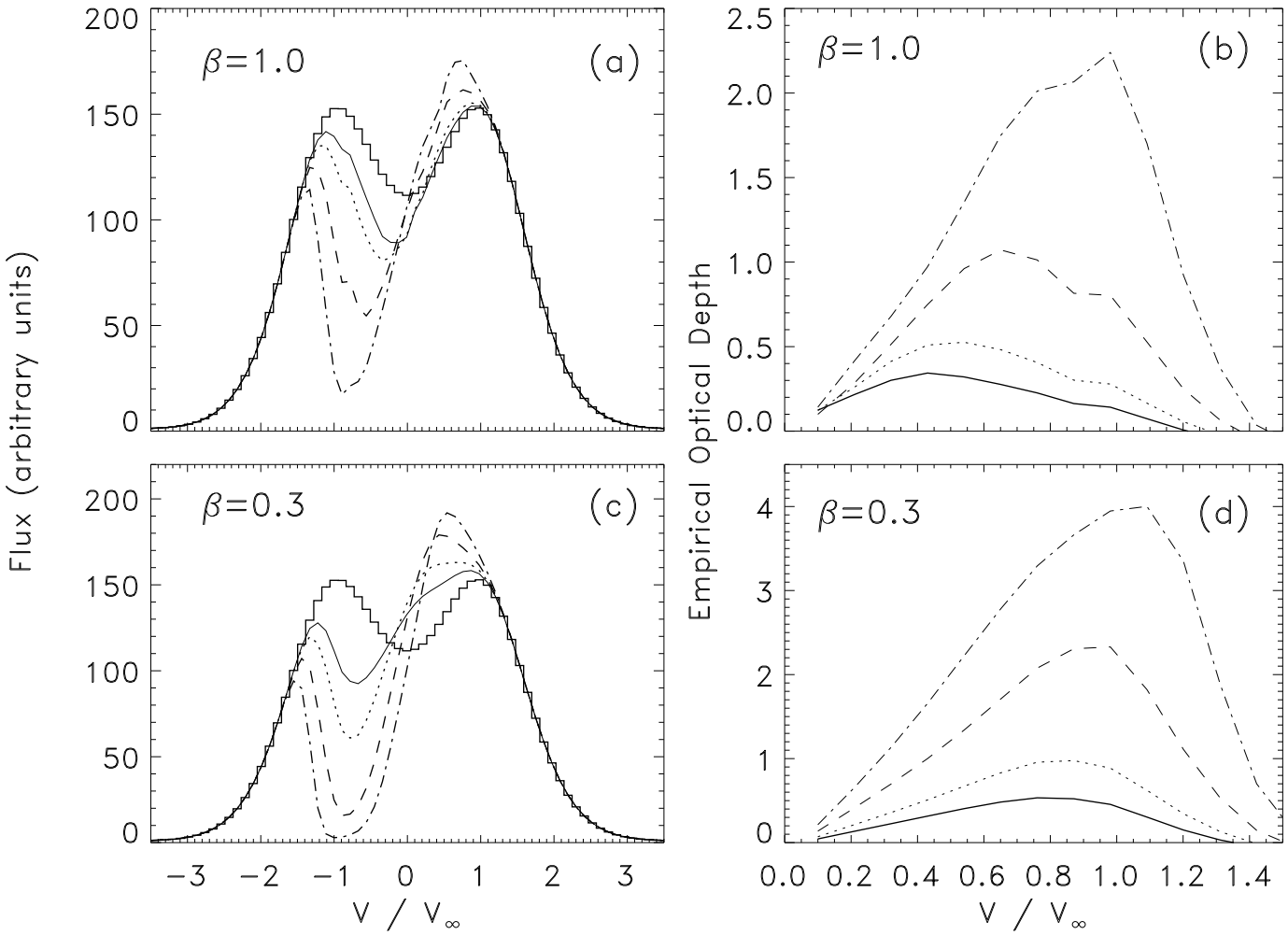

FIG. 13.—(*a* and *c*) SEI profiles for different values of β and total wind optical depth. The line profile at the base of the wind (*solid histograms*) is similar to that expected for the O I (UV 2) lines in α Tau. The integrated wind opacities are 0.5 (*solid lines*), 1.0 (*dotted lines*), 3.0 (*dashed lines*), and 10.0 (*dot-dashed lines*). The turbulence has a value $w_D = v_D/v_\infty = 0.3$. (*b* and *d*) Empirical optical depths derived by applying the reflection analysis described in § 7.3 to the computer profiles in (*a*) and (*c*).

scatter photons only at low velocities. As the wind opacity increases, the higher velocity layers become important and the position of the central absorption feature moves progressively toward the blue (Fig. 13*a*). The excess emission on the red side of the line is clearly visible and increases as the depth of the wind increases, as expected. For $\beta = 0.3$, the opacity peaks at the terminal velocity, and the majority of the scattering occurs at this velocity, regardless of the depth of the wind. Thus, the position of the central absorption remains constant (Fig. 13*c*).

Figures 13*b* and 13*d* show the results of a reflection analysis on the calculated profiles, similar to that discussed in § 7.3 for the observed profiles. While the overall shapes are similar in the two figures, there are differences in the detail. For example, in Figure 13*b* the drift in the peak opacity from low to high velocities with increasing total wind opacity is clearly evident. The velocity of the peak opacity in Figure 13*d* is much more constant. Note also that the empirical opacities are larger for the case of $\beta = 0.3$ than for $\beta = 1$, even though the total wind opacities used in the calculations were the same. This is caused by the fact that scattering of blue photons into the line core partially cancels the effects of wind opacities at small velocities, so that a given opacity at high velocities has a larger effect on the profile than opacity at low velocities.

In Figure 13 we assumed a turbulence parameter ($w_D = v_D/v_\infty$) of 0.3. This turbulence causes the effects of the wind to extend beyond the terminal velocity and also acts to couple layers of the atmosphere moving at different velocities, thereby reducing the effect of the wind acceleration parameter (β) on the line profile. This is illustrated in Figure 14. For low turbulence, the empirical opacities derived from the reflection analysis are dramatically different for the cases of $\beta = 0.3$ and 1.0. As the turbulence increases, the empirical relations for the two values of β become more symmetrical and begin to resemble one another in shape. An increase in the turbulence also extends the wind scattering efficiency into the red side of the line and influences the number of photons scattered into the line core. This is particularly evident in Figure 14*a*, where a wind with $\beta = 1.0$, $\tau = 3$, and $w_D = 0.5$ has completely eliminated the photons scattered into the red peak.

9.2. *Modeling the Stellar Winds*

The goal of the wind-modeling process was to determine the characteristics of a wind that could account for the profile shapes of all of the lines for which a wind signature was observed. For α Tau, we used the Fe II λ2755 line as well as the three O I (UV 2) lines. The Mg II (UV 1) lines could not be used because of the strong interstellar absorp-

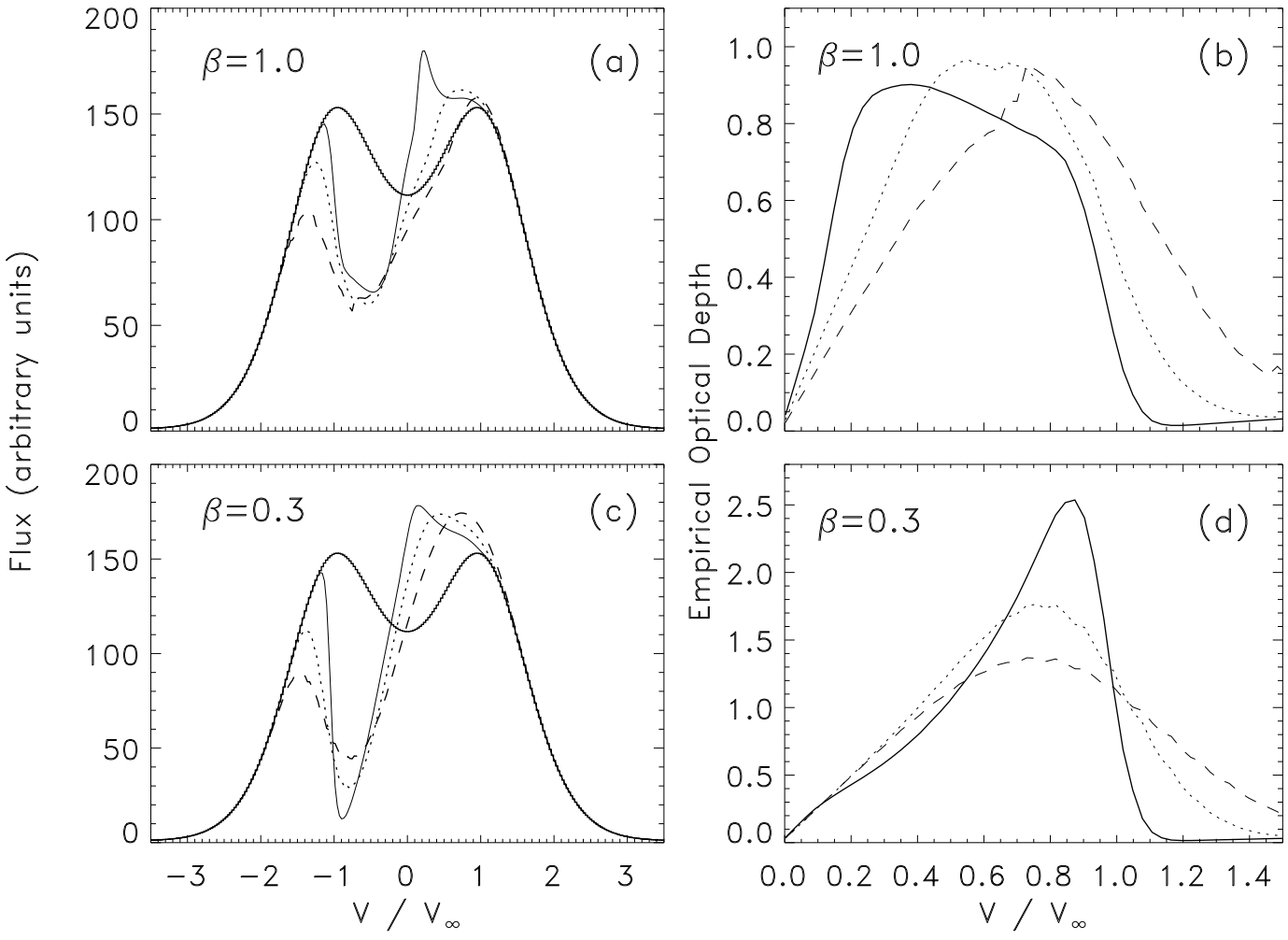

FIG. 14.—(*a* and *c*) Effects of turbulence on the line profile for specified values of β and a total wind optical depth of 3. The turbulence parameter, $w_D = v_D/v_\infty$, has values of 0.1 (*solid lines*), 0.3 (*dotted lines*), and 0.5 (*dashed lines*). The intrinsic profile is shown with the thick solid line. (*b* and *d*) Empirical optical depths derived by applying the reflection analysis described in § 7.3 to the computed profiles.

tion feature centered near the wind terminal velocity. The intrinsic profiles at the base of the wind in α Tau consisted of two components. The first was an emission feature that matched the far wings of the observed lines and was centered at a velocity of $+2$ km s^{-1} with respect to the stellar rest frame. This was consistent with the emission velocities calculated for the various Fe II lines (see § 7.2). The second was an absorption feature centered at the same RV as the emission (so that the profile was constrained to be symmetrical) and having a depth and width that was adjusted during the modeling process until an acceptable fit to the observations was obtained.

An initial guess of the wind parameters can be obtained from the reflection analysis in Figure 9*a*. The maximum optical depth in all three lines occurs at ~ 30 km s^{-1}, which we took as the initial guess for the terminal velocity. The opacity also extends to at least 55 km s^{-1}, implying a substantial turbulence. The fact that the position of the absorption feature moves to the blue in lines with increasing strength (Fig. 7*a*) also suggests that the opacity decreases with velocity, i.e., that β is ≥ 0.5. Starting with O I λ1304, we iterated values of β, v_∞, $\tau_{\rm tot}$, and w_D for the wind and the depth and width of the absorption feature in the intrinsic profile until an acceptable fit was obtained. In this fitting process, values for v_∞ and w_D could be established with a reasonable degree of confidence. However, it was possible to get consistent fits for values of β ranging from 0.5 to 0.8 by slightly adjusting the character of the intrinsic profile and the total wind opacity. This ambiguity in β is due to the large turbulence, as discussed in § 9.1. Once a refined guess to the wind parameters was obtained, the parameters were applied to the analysis of the other line profiles as a consistency check. The resultant fits are shown in Figure 15 and represent a wind with $v_\infty = 30$ km s^{-1}, $v_D = 24$ km s^{-1}, and $\beta = 0.6 \pm 0.2$. The deduced optical depth for each of the lines is shown in Table 7 and is approximately consistent with the relative strengths of the lines.

The reflection analysis for γ Dra (Fig. 9*b*) shows a skewed distribution, which peaks at ~ 55 km s^{-1}. The distribution [particularly for the two Mg II (UV 2) lines] is very similar to the solid line in Figure 14*d*, which implies that β is small and that there is relatively little turbulence. We again used the O I λ1304 line in the initial fit and then extended the analysis to other lines affected by the wind. The best fits are shown in Figures 16 and 17 and represent a wind with $v_\infty = 67$ km s^{-1}, $v_D = 12$ km s^{-1}, and $\beta = 0.35 \pm 0.1$. The small level of turbulence allowed us to deduce β with more accuracy than was possible in α Tau. The value of β is near the lower limit of the value deduced by Harper et al. (1995) for the hybrid star α TrA and is considerably smaller than

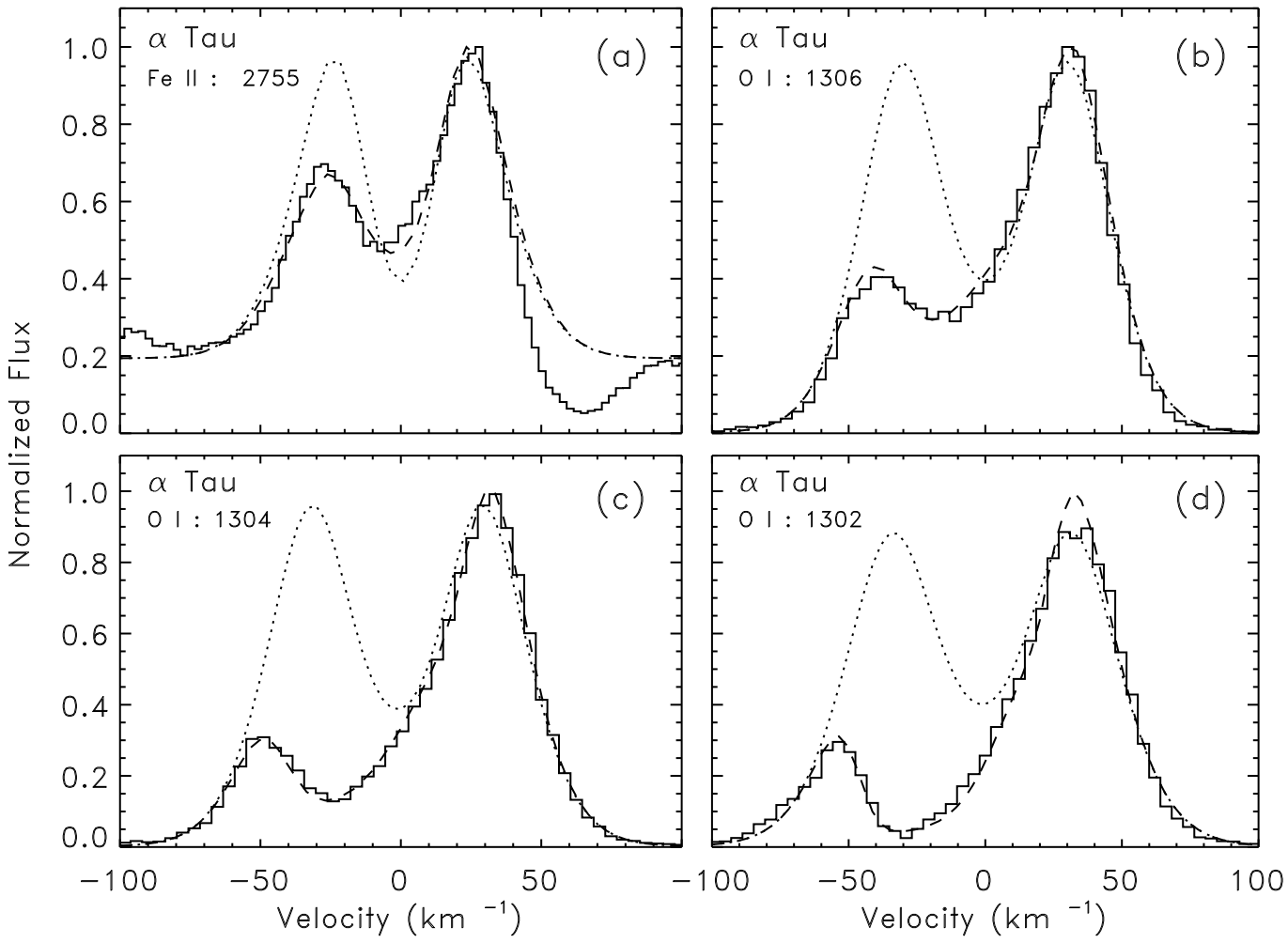

FIG. 15.—Observed α Tau profiles (*solid histograms*) for Fe II λ2755 and the three O I (UV 2) lines compared with simulated profiles (*dashed lines*) deduced from the SEI code. The assumed profiles at the base of the wind (*dotted lines*) were derived as explained in § 9.2. The wind model assumes $v_\infty = 30$ km s^{-1}, $\beta = 0.6$, and $v_D = 24$ km s^{-1}.

TABLE 7

WIND PROPERTIES

WAVELENGTH (Å)	LINE ID	*gf*	TOTAL WIND OPACITY		$\dot{M}$ (10^{-11} $M_\odot$ yr^{-1})	
			α Tau	γ Dra	α Tau	γ Dra
1302.174.....	O I (UV 2)	0.24	15.0[a]	2.0[b]	1.6[a]	0.97[b]
1304.858.....	O I (UV 2)	0.15	7.0[a]	1.3[b]	1.2[a]	1.0[b]
1306.023.....	O I (UV 2)	0.05	3.0[a]	0.5[b]	1.6[a]	1.2[b]
2795.523.....	Mg II (UV 1)	1.23	...	5.0[b]	...	1.3[b]
			...	3.5[a]	...	0.16[a]
2802.698.....	Mg II (UV 1)	0.61	...	2.5[b]	...	1.3[b]
			...	1.5[a]	...	0.13[a]

[a] Wind component with $\beta = 0.6$.
[b] Wind component with $\beta = 0.35$.

the values of 2.5–3.5 found for ζ Aur systems (Kirsch & Baade 1994).

While the fits to the Fe II and O I lines in Figure 16 are quite good, the fits to the Mg II h and k lines (Fig. 17; *dashed lines*) do not account for an excess absorption between 0 and -40 km s^{-1} in both of the lines. Since this discrepancy occurs at roughly the same velocity range in both lines, it is most likely caused by an excess Mg II absorption rather than mutilation by other elements in the circumstellar shell. The most likely explanation, therefore, is the existence of an additional low-velocity wind component with a sufficiently low column mass that it is not detectable in the lower opacity lines. To check this assertion, we used the initial fit (i.e., Fig. 17, *dashed lines*) as the input to a second SEI calculation in which the wind character was the same as that deduced for α Tau (i.e., $\beta = 0.6$, $v_D = 24$ km s^{-1}, and $v_\infty = 30$ km s^{-1}). The resultant fits are shown by the dotted line in Figure 17 and accurately reproduce the observed profile. The deduced optical depths for this wind component were 3.5 ± 0.5 for Mg II k and 1.5 ± 0.3 for the Mg II

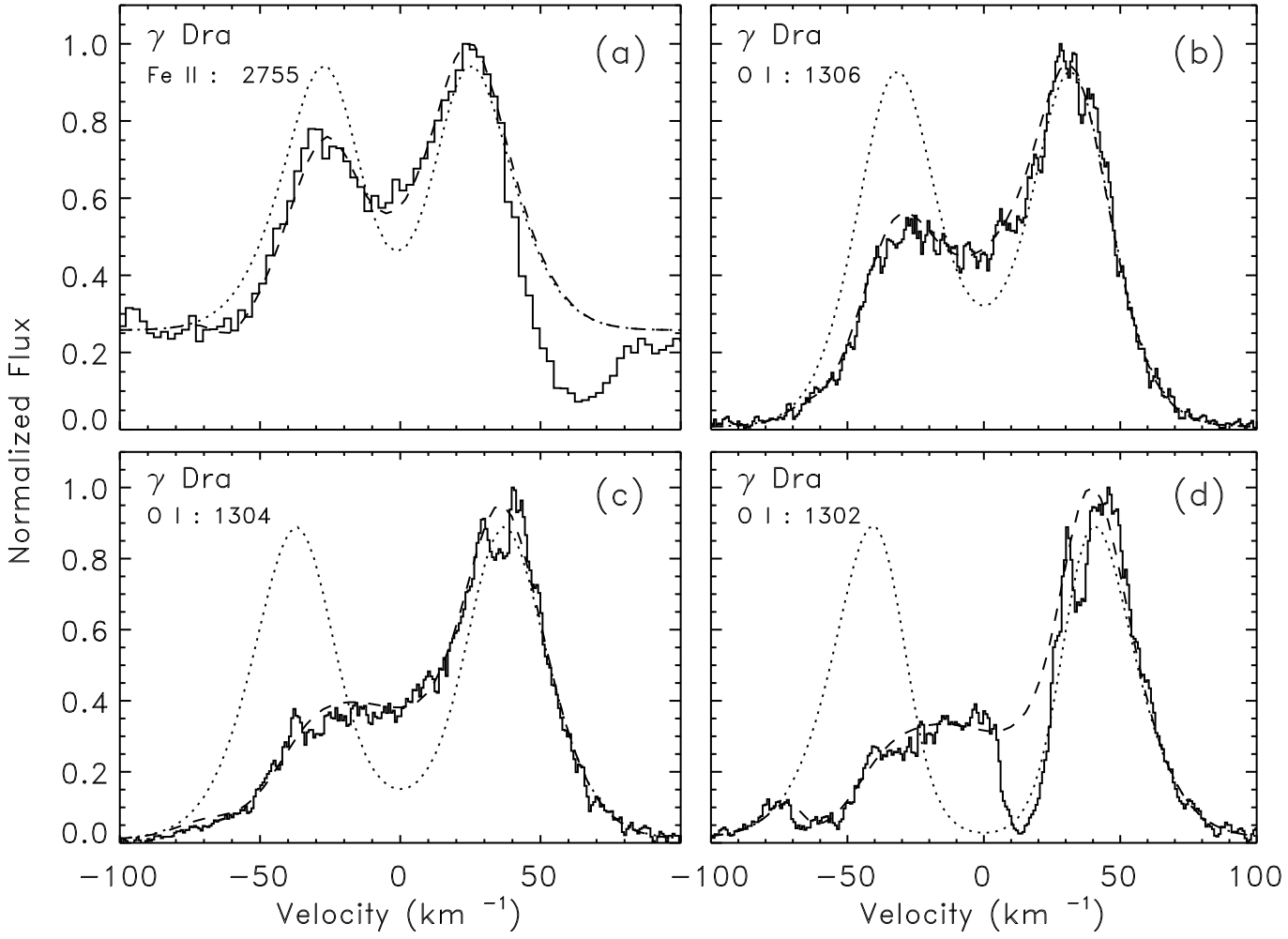

FIG. 16.—Observed γ Dra profiles (*solid histograms*) for Fe II λ2755 and the three O I (UV 2) lines compared with simulated profiles (*dashed lines*) deduced from the SEI code. The assumed profiles at the base of the wind (*dotted lines*) were derived as explained in § 9.2. The wind model assumes $v_\infty = 67$ km s^{-1}, $\beta = 0.4$, and $w_D = 0.1$.

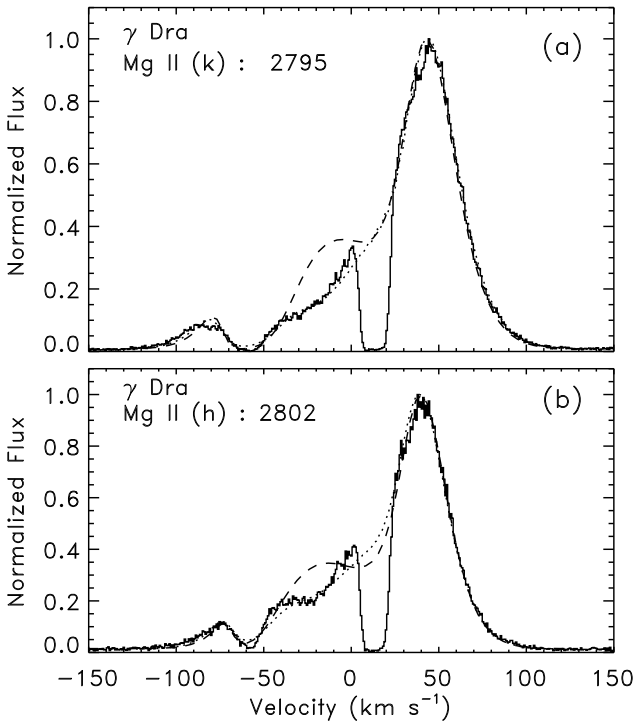

FIG. 17.—Comparison of the observed γ Dra Mg II (UV 1) profiles (*solid lines*) with simulated profiles deduced from the SEI code. The fit assuming a single wind component identical to that used in Fig. 16 is given by the dashed lines. The dotted lines show a fit when a second, low-velocity wind component has been added. The second component has the same properties as those deduced for α Tau. The assumed profiles at the base of the wind are similar to those shown in Fig. 16.

h line, which are somewhat smaller than that for the high-speed wind.

The shapes of the intrinsic chromospheric profiles at the base of the wind are one of the byproducts of our analysis. Note in Figures 15 and 16 that the widths of both the emission and the absorption components of the deduced profiles increase with increasing line strength in both stars. However, while the depth of the absorption features in α Tau are relatively constant, the depths increase dramatically with line strength in γ Dra. This implies a substantial difference in the structure of the middle to upper chromosphere, which is presumably where the stellar wind is initiated.

At this point, it should also be noted that the observed profiles can be reproduced simply by assuming a symmetric intrinsic profile convolved with the effects of an expanding wind, without recourse to downflowing material. However, when applying the Gaussian fitting procedure discussed in § 7.2, we required both a blue and a red absorption component to fit the observed profiles. This is similar to the situation found for γ Cru (Carpenter et al. 1995), where it was suggested that the multiple absorption components *might* represent a circulation pattern. It is now evident that this suggestion is not true and that the red absorption feature is simply the residual of the absorption feature in the intrinsic chromospheric profile.

The mass loss from the stellar winds can now be calculated from the deduced wind characteristics. Following Snow (1981), we combine equations (4) and (6) to produce an expression for the mass-loss rate ($\dot{M}$) in terms of the unitless variables $x\,(=R/R_*)$ and $w\,(=V/V_\infty)$:

$$\dot{M} = \frac{4mc}{e^2}\,\frac{\mu m_{\rm H} v_\infty^2 R_* U}{gf\lambda_0 I A_E}\,\tau(w)\left(x^2 w\,\frac{dw}{dx}\right), \qquad (7)$$

where $m_{\rm H}$ is the atomic mass of hydrogen, μ is the mean atomic weight, I is the ionization fraction of the observed ionic species, and A_E is the abundance of the observed element with respect to hydrogen. At $w = 0.5$, the function $x^2 w(dw/dx)$ has a value of ~ 0.5 for β between 0.5 and 1. Using this in equation (7) then gives the expression

$$\dot{M} = 6.1 \times 10^{-19}\tau(w = 0.5)\,\frac{v_\infty^2 R_* U}{gf\lambda_0 I A_E}, \qquad (8)$$

where $\dot{M}$ is the mass loss in $M_\odot$ yr^{-1}, R_* is given in units of $R_\odot$, v_∞ in units of km s^{-1}, and λ_0 in Å. Table 7 presents the mass-loss rates deduced from each of the fitted lines using the average wind characteristics and the stellar parameters presented in § 3. In these calculations, we have taken the oxygen abundance for α Tau to be $A_E = 5.9 \times 10^{-4}$ (Smith & Lambert 1985), which is slightly smaller than the value for the Sun. The solar oxygen abundance ($A_E = 8.3 \times 10^{-4}$; Lambert 1978) is assumed for γ Dra. In both cases, the ionic fraction of O I is assumed to be 1 throughout the atmosphere. The justification for this is discussed by Carlsson & Judge (1993). It is further assumed that the Mg II abundance in γ Dra is solar, with $A_E = 3.3 \times 10^{-5}$ (Lang 1997), and that Mg II dominates throughout the atmosphere, as postulated by Harper et al. (1995) in modeling α TrA. Note that the mass loss predicted from the O I lines is about the same for α Tau and γ Dra, despite the differences in the terminal velocities of the wind. The mass loss from the low-speed wind component in γ Dra, however, is only about 10% that of the high-speed wind.

10. SUMMARY AND CONCLUSIONS

We report on the analysis of GHRS observations of the normal K5 III star α Tau. These data show the presence of an energetic chromosphere, with strong emission in Fe II, Mg II, and O I, as well as a pronounced UV continuum, which is orders of magnitude stronger than that expected from the photosphere and has a total radiative output that is substantially larger than that arising from the chromospheric emission lines. Chromospheric turbulence, as deduced from the C II] and other optically thin emission lines, is found to have an asymmetric velocity distribution with local motions directed preferentially either along or tangential to the radial direction with an amplitude of ~ 26 km s^{-1}. This is somewhat smaller than the values previously found for the M3.4 III star γ Cru, which was the subject of a previous paper in this series (Carpenter et al. 1995). The wind in α Tau is also considerably weaker than in γ Cru since its signature appears only in the strongest of the observed Fe II line profiles. The nature of this wind was found to be variable in time, showing a slight decrease in velocity with increasing chromospheric density and line fluxes. It is interesting to note that the chromospheric turbulence showed no variation at all in connection with the observed atmospheric restructuring.

A comparison of α Tau with the K5 III hybrid star γ Dra shows remarkable similarities in their photospheres and

lower chromospheres. These two stars not only have very similar spectral types and optical colors, but their UV continuum fluxes are similar down to wavelengths of at least 1300 Å. The turbulent velocities, as indicated by the C II] intercombination lines, as well as the chromospheric densities deduced from the C II] line ratios, are essentially identical for the two stars. The surface fluxes and line profiles for all emission lines formed in the lower to mid-chromosphere (e.g., C II, Si I, Co II, and Fe II) are similar, with lines in γ Dra being 40%–65% stronger than those in α Tau at the time the data were taken. However, given the moderately large flux variations reported here for α Tau and the known chromospheric variability in hybrid stars (see, e.g., Brown et al. 1996) this flux difference may not be significant. The main observed difference in the photosphere and lower chromosphere of the two stars is the existence in α Tau of dense, cool material, which is responsible for the numerous fluorescent features in its spectrum.

The detection of C IV emission in α Tau clearly shows that the mere presence of such emission can no longer be considered a defining characteristic of a hybrid star. Further, while the C IV surface flux from the 1996 observation of γ Dra was more than 120 ergs cm^{-2} s^{-1}, Simon, Linsky, & Stencel (1982) have reported an upper limit of only 30 ergs cm^{-2} s^{-1} from early *IUE* observations of γ Dra. If this upper limit is valid, then it suggests that the transition-region flux can vary dramatically in the hybrid stars, so that the moderately large surface flux ratio between γ Dra and α Tau ($=3.5 \pm 1$) does not necessarily imply that the hybrid star has intrinsically stronger transition region emission than the noncoronal star.

It is not until we reach the upper chromosphere, probed by the O I and Mg II lines, that significant differences in the stars appear. These lines are dominated by the effects of stellar winds, which have a terminal velocity of 30 km s^{-1} in α Tau and 67 km s^{-1} in γ Dra. In α Tau, this wind probably accelerates more slowly ($\beta = 0.6$ vs. 0.35) and has a higher turbulence (25 km s^{-1} vs. 7 km s^{-1}) than in γ Dra. However, despite these differences, the mass-loss rate for the two stars may be about the same. There is also some evidence for secondary wind components in these stars, a high-speed wind in α Tau and a low-speed component in γ Dra. In each case, the mass loss from these secondary components is only a small fraction of that from the main wind.

From this study, we can therefore conclude that (1) there is probably no relation between the strength of hot transition-region plasma and the mass-loss rate from a star and (2) the amount of chromospheric turbulence is *not* the characteristic that determines the properties of the stellar wind, though it is very possibly associated with the chromospheric heating.

Overall, the observations are consistent with the picture provided by Judge & Stencel (1991), who suggest that the mechanism heating the chromosphere is essentially decoupled from the mechanism that drives the wind. According to their model, the energy that drives both atmospheric heating and wind acceleration is contained in waves that are generated by convective motions and/or pulsations low in the stellar atmosphere. High-frequency waves are damped in the chromosphere and produce the heating while lower frequency waves pass through the lower chromosphere and accelerate the wind. The difference between the two stars may therefore lie in the nature of these convective and/or pulsational motions, particularly in regard to the low-frequency part of the spectrum. As suggested in § 3, the evolutionary state of the two stars may be different, with γ Dra being on the AGB while α Tau is still on the RGB (or vice versa). The resultant differences in the internal structures of the stars may then be sufficient to account for supposed differences in the wave spectrum. Similar arguments involving low-frequency turbulence have also been used by Mullan & Fleming (1996) to account for the differences in coronal heating in dMe stars. Unfortunately, very little is currently known about the effects of stellar evolution on the frequency spectrum of convective motions.

This work was supported by NASA through STScI GO grants 5358 and 6068. The GHRS observations were obtained by the NASA/ESA *Hubble Space Telescope*, which is operated at the Space Telescope Science Institute by the Association of Universities for Research in Astronomy, Inc., under NASA contract NAS 5-26555.

REFERENCES

Ayres, T. R., Brown, A., Harper, G. M., Bennett, P. D., Linsky, J. L., Carpenter, K., & Robinson, R. 1998, ApJ, 491, 876
Blackwell, D. E., Petford, A. D., Arribas, S., Haddock, D., & Selby, M. J. 1990, A&A, 232, 396
Bonnell, J. T., & Bell, R. A. 1993, MNRAS, 264, 319
Brown, A., Carpenter, K. G., Robinson, R. D., Harper, G. M., Deeney, B. D., & Ayres, T. R. 1995, BAAS, 187, 103.03
Brown, A., Deeney, B. D., Ayres, T. R., Veale, A., & Bennett, P. D. 1996, ApJS, 107, 263
Carlsson, M., & Judge, P. G. 1993, ApJ, 402, 344
Carpenter, K. G., & Robinson, R. D. 1995, in ASP Conf. Proc. 81, Workshop on Laboratory & Astronomical High-Resolution Spectra, ed. A. J. Sauval, R. Blomme, & N. Greuesse (San Francisco: ASP), 559
———. 1997, ApJ, 479, 970
Carpenter, K. G., Robinson, R. D., & Judge, P. G. 1995, ApJ, 444, 424
Carpenter, K. G., Robinson, R. D., Wahlgren, G. M., Ake, T. B., Ebbets, D. C., Linsky, J. L., Brown, A., & Walter, F. M. 1991, ApJ, 377, L45
Carpenter, K. G., Robinson, R. D., Wahlgren, G. M., Linsky, J. L., & Brown, A. 1994, ApJ, 428, 329
Castor, J. I. 1970, MNRAS, 149, 111
Castor, J. I., & Lamers, H. J. G. L. M. 1979, ApJS, 39, 481
Cayrel de Strobel, G., Hauck, B., Francois, P., Thevenin, F., Friel, E., Mermilloid, M., & Borde, S. 1992, A&AS, 95, 273
Cohen, M., Witteborn, F. C., Carbon, D. F., Davis, J. K., Wooden, D. H., & Bregman, J. D. 1996, AJ, 112, 2274
Di Benedetto, G. P. 1993, A&A, 270, 315
Drake, S. A., Brown, A., & Linsky, J. L. 1984, ApJ, 284, 774
el Eid, M. F. 1994, A&A, 285, 915
Flower, P. J. 1996, ApJ, 469, 355
Gray, D. F. 1992, The Observation and Analysis of Stellar Photospheres (Cambridge: Cambridge Univ. Press)
Hamann, W.-R. 1980, A&A, 84, 342
Harper, G. M., Wood, B. E., Linsky, J. L., Bennett, P. D., Ayres, T. R., & Brown, A. 1995, ApJ, 452, 407
Hartmann, L., Dupree, A. K., & Raymond, J. C. 1980, ApJ, 236, L143
Heap, S. R., et al. 1995, PASP, 107, 871
Jaschek, C. 1982, The Bright Star Catalogue (New Haven: Yale Univ. Obs.)
Judge, P. G. 1986, MNRAS, 223, 239
Judge, P. G., & Cuntz, M. 1993, ApJ, 409, 776
Judge, P. G., & Stencel, R. E. 1991, ApJ, 371, 357
Kelch, W. L., Linsky, J. L., Basri, G. S., Chiu, H.-Y., Chang, S.-H., Maran, S. P., & Furenlid, F. 1978, ApJ, 220, 962
Kirsch, T., & Baade, R. 1994, A&A, 291, 535
Kovacs, N. 1983, A&A, 120, 21
Kurucz, R. L. 1992, in IAU Symp. 149, The Stellar Populations of Galaxies, ed. B. Barbuy & A. Renzini (Dordrect: Kluwer), 225
Lambert, D. L. 1978, MNRAS, 182, 249
Lamers, H. J. G. L. M., Cerruti-Sola, M., & Perinotto, M. 1987, ApJ, 314, 726
Lang, K. R. 1997, Astrophysical Formulae. A Compendium for the Physicist and Astrophysicist (3d ed.; Berlin: Springer)

Lennon, D. J., Dufton, P. L., Hibbert, A., & Kingston, A. E. 1985, ApJ, 294, 200
Lindler, D., & Heap, S. R. 1995, Calibrating the *Hubble Space Telescope*: Post Servicing Mission, Workshop Proc., ed A. Koratkar & C. Leitherer (Baltimore: STScI), 202
Linsky, J. L. 1991, in Mechanisms of Chromospheric and Coronal Heating, ed P. Ulmschneider, E. R. Priest, & R. Rosner (New York: Springer), 166
Linsky, J. L., & Haisch, B. M. 1979, ApJ, 229, L27
McMurry, A. D., Jordan, C., Carpenter, K. G., & Robinson, R. D. 1998, in ASP Conf. Proc., Cool Stars, Stellar Systems, and the Sun, 10th Cambridge Workshop, ed. R. A. Donahue & J. A. Bookbinder (San Francisco: ASP), 1293
McMurry, A. D., Jordan, C., Rowe, A. K., Carpenter, K. G., & Robinson, R. D. 1996, in ASP Conf. Proc. 109, Cool Stars, Stellar Systems, and the Sun, 9th Cambridge Workshop, ed. R. Pallavicini & A. K. Dupree (San Francisco: ASP), 271
McWilliams, A. 1990, ApJS, 74, 1075
Morossi, C., Franchini, M., Malagnini, M. L., Kurucz, R. L., & Buser, R. 1993, A&A, 277, 173
Mullan, D. J., Carpenter, K. G., & Robinson, R. D. 1998, ApJ, 495, 927
Mullan, D. J., & Fleming, T. A. 1996, ApJ, 464, 890
Robinson, R. D., & Carpenter, K. G. 1995, ApJ, 442, 328
Rutten, R. G. M., & Pylyser, E. 1988, A&A, 191, 227
Simon, T., Linsky, J. L., & Stencel, R. E. 1982, ApJ, 257, 225
Smith, V. V., & Lambert, D. L. 1985, ApJ, 294, 326
Snow, T. P., Jr. 1981, ApJ, 251, 139
Taylor, B. J. 1991, ApJS, 76, 715
Ulmschneider, P. 1991, in Mechanisms of Chromospheric and Coronal Heating, ed. P. Ulmschneider, E. R. Priest, & R. Rosner (New York: Springer), 328
Wood, B. E., & Linsky, J. L. 1998, ApJ, 492, 788